A&A 508, 1141–1159 (2009)
DOI: 10.1051/0004-6361/20078872


Astronomy & Astrophysics

# Evolution of the early-type galaxy fraction in clusters since $z = 0.8$⋆,⋆⋆

L. Simard[1], D. Clowe[2], V. Desai[3], J. J. Dalcanton[4], A. von der Linden[5,6], B. M. Poggianti[7], S. D. M. White[6], A. Aragón-Salamanca[8], G. De Lucia[6,9], C. Halliday[10], P. Jablonka[11], B. Milvang-Jensen[12,13], R. P. Saglia[14], R. Pelló[15], G. H. Rudnick[16,17], and D. Zaritsky[18]

*(Affiliations can be found after the references)*

Received 18 October 2007 / Accepted 6 October 2009

**ABSTRACT**

We study the morphological content of a large sample of high-redshift clusters to determine its dependence on cluster mass and redshift. Quantitative morphologies are based on PSF-convolved, 2D bulge+disk decompositions of cluster and field galaxies on deep Very Large Telescope FORS2 images of eighteen, optically-selected galaxy clusters at $0.45 < z < 0.80$ observed as part of the ESO Distant Cluster Survey ("EDisCS"). Morphological content is characterized by the early-type galaxy fraction $f_{\rm et}$, and early-type galaxies are objectively selected based on their bulge fraction and image smoothness. This quantitative selection is equivalent to selecting galaxies visually classified as E *or* S0. Changes in early-type fractions as a function of cluster velocity dispersion, redshift and star-formation activity are studied. A set of 158 clusters extracted from the Sloan Digital Sky Survey is analyzed exactly as the distant EDisCS sample to provide a robust local comparison. We also compare our results to a set of clusters from the Millennium Simulation. Our main results are: (1) the early-type fractions of the SDSS and EDisCS clusters exhibit no clear trend as a function of cluster velocity dispersion. (2) Mid-$z$ EDisCS clusters around $\sigma = 500$ km s$^{-1}$ have $f_{\rm et} \simeq 0.5$ whereas high-$z$ EDisCS clusters have $f_{\rm et} \simeq 0.4$. This represents a ∼25% increase over a time interval of 2 Gyr. (3) There is a marked difference in the morphological content of EDisCS and SDSS clusters. None of the EDisCS clusters have early-type galaxy fractions greater than 0.6 whereas half of the SDSS clusters lie above this value. This difference is seen in clusters of all velocity dispersions. (4) There is a strong and clear correlation between morphology and star formation activity in SDSS and EDisCS clusters in the sense that decreasing fractions of [OII] emitters are tracked by increasing early-type fractions. This correlation holds independent of cluster velocity dispersion and redshift even though the fraction of [OII] emitters decreases from $z \sim 0.8$ to $z \sim 0.06$ in all environments. Our results pose an interesting challenge to structural transformation and star formation quenching processes that strongly depend on the global cluster environment (e.g., a dense ICM) and suggest that cluster membership may be of lesser importance than other variables in determining galaxy properties.

**Key words.** galaxies: fundamental parameters – galaxies: evolution – galaxies: clusters: general

## 1. Introduction

Our current paradigm for the origin of galaxy morphologies rests upon hierarchical mass assembly (e.g., Steinmetz & Navarro 2002), and many transformational processes are at work throughout the evolutionary histories of galaxies. Some determine the main structural traits (e.g., disk versus spheroid) while others only influence properties such as color and star-formation rates. Disk galaxy collisions lead to the formation of elliptical galaxies (Spitzer & Baade 1951; Toomre & Toomre 1972; Farouki & Shapiro 1982; Negroponte & White 1983; Barnes & Hernquist 1992, 1996; Mihos & Hernquist 1996), and the extreme example of this process is the build-up of the most massive galaxies in the Universe at the cores of galaxy clusters through the accretion of cluster members. Disks can also be transformed into spheroidals by tidal shocks as they are harassed by the cluster gravitational potential (Farouki & Shapiro 1981; Moore et al. 1996, 1998). Harassment inflicts more damage to low luminosity galaxies because of their slowly rising rotation curves and their low density cores. Galaxies can be stripped of their internal gas and external supply through ram pressure exerted by the intracluster medium (Gunn & Gott 1972; Larson et al. 1980; Quilis et al. 2000), and the result is a "quenching" (or "strangulation") of their star formation that leads to a rapid reddening of their colours (also see Martig et al. 2009). The task of isolating observationally the effects of a given process has remained a major challenge to this day.

Many processes affecting galaxy morphologies are clearly environmentally-driven, and galaxy clusters are therefore ideal laboratories in which to study all of them. The dynamical state of a cluster, which can be observationally characterized by measuring mass and substructures, should be related to its morphological content. For example, the number of interactions/collisions suffered by a given galaxy should depend on local number density and the time it has spent within the cluster. Dynamically young clusters with a high degree of subclustering should

⋆ Based on observations obtained in visitor and service modes at the ESO Very Large Telescope (VLT) as part of the Large Programme 166.A-0162 (the ESO Distant Cluster Survey). Also based on observations made with the NASA/ESA Hubble Space Telescope, obtained at the Space Telescope Science Institute, which is operated by the Association of Universities for Research in Astronomy, Inc., under NASA contract NAS 5-26555. These observations are associated with proposal 9476. Support for this proposal was provided by NASA through a grant from the Space Telescope Science Institute.

⋆⋆ Table 4 is only available in electronic form at http://www.aanda.org

contain large numbers of galaxies that are infalling for the first time. More massive clusters will contain more galaxies, but they will also have higher galaxy-galaxy relative velocities that may impede merging (Lubin et al. 2002). Spheroidal/elliptical galaxies will preferentially be formed in environments where the balance between number density and velocity dispersions is optimal, but it is still not clear where this optimal balance lies. Cluster masses can be estimated from their galaxy internal velocity dispersion (Rood et al. 1972; Dressler 1984; Carlberg et al. 1997; Tran et al. 1999; Borgani et al. 1999; Lubin et al. 2002), through weak-lensing shear (Kaiser & Squires 1993; Schneider & Seitz 1995; Hoekstra et al. 2000; Clowe et al. 2006) or through analysis of their hot X-ray emitting atmospheres (e.g., Allen 1998), and it will be used here as the main independent variable against which morphological content will be studied.

The morphological content of high-redshift clusters is most often characterized by the fraction $f_{\rm E+S0}$ of early-type galaxies they contain (Dressler et al. 1997; van Dokkum et al. 2000; Fasano et al. 2000; van Dokkum et al. 2001; Lubin et al. 2002; Holden et al. 2004; Smith et al. 2005; Postman et al. 2005; Desai et al. 2007; Poggianti et al. 2009b). The bulk of the data available so far is based on visual classification. "Early-type" galaxies are defined in terms of visual classifications as galaxies with E or S0 Hubble types. A compilation of early-type fractions taken from the literature (van Dokkum et al. 2000) shows a dramatic increase of the early-type fractions as a function of decreasing redshift from values around 0.4−0.5 at $z \sim 1$ to values around 0.8 in the local Universe. However, the interpretation of this trend is not entirely clear as others (e.g., Dressler et al. 1997; Fasano et al. 2000; Desai et al. 2007; Poggianti et al. 2009b) have reported that the fraction of E's remains unchanged as a function of redshift and that the observed changes in early-type fractions are entirely due to the S0 cluster populations. S0 populations were observed to grow at the expense of the spiral population (Smith et al. 2005; Postman et al. 2005; Moran et al. 2007; Poggianti et al. 2009b) although others (e.g., Holden et al. 2009) have argued for no evolution in the relative fraction of ellipticals and S0s with redshift. Smith et al. (2005) and Postman et al. (2005) show that the evolution of $f_{\rm E+S0}$ is in fact a function of both lookback time (redshift) and projected galaxy density. They find $f_{\rm E+S0}$ stays constant at 0.4 over the range $1 < t_{\rm lookback} < 8$ Gyr for projected galaxy densities $\Sigma < 10$ Mpc$^{-2}$. For high density environments ($\Sigma = 1000$ Mpc$^{-2}$), $f_{\rm E+S0}$ decreases from 0.9 to 0.7. At fixed lookback time, $f_{\rm E+S0}$ varies by a factor of 1.8 from low to high densities at $t_{\rm lookback} = 8$ Gyr and by a factor of 2.3 at $t_{\rm lookback} = 1$ Gyr. The difference between low and high density environments thus increases with decreasing lookback time. Both studies indicate that the transition between low and high densities occurs at 0.6 $R_{200}$ ($R_{200}$ is the projected radius delimiting a sphere with interior mean density 200 times the critical density at the cluster redshift, see Eq. (1)). Postman et al. (2005) also find that $f_{\rm E+S0}$ does not change with cluster velocity dispersion for massive clusters ($\sigma > 800$ km s$^{-1}$). The data for one of their clusters also suggest that $f_{\rm E+S0}$ decreases for lower mass systems. This trend would be consistent with observations of $f_{\rm E+S0}$ in groups that show a strong trend of decreasing $f_{\rm E+S0}$ versus decreasing $\sigma$ (Zabludoff & Mulchaey 1998). Finally, $f_{\rm E+S0}$ seems to correlate with cluster X-ray luminosity at the $2-3\sigma$ level (Postman et al. 2005).

Recent works on stellar mass-selected cluster galaxy samples (Holden et al. 2007; van der Wel et al. 2007) paint a different picture. The fractions of E+S0 galaxies in clusters, groups and the field do not appear to have changed significantly from $z \sim 0.8$ to $z \sim 0.03$ for galaxies with masses greater than $4 \times 10^{10}\ M_{\odot}$. The mass-selected early-type fraction remains around 90% in dense environments ($\Sigma > 500$ gal Mpc$^{-2}$) and 45% in groups and the field. These results show that the morphology-density relation of galaxies more massive than 0.5 $M_*$ has changed little since $z \sim 0.8$ and that the trend in morphological evolution seen in luminosity-selected samples must be due to lower mass galaxies. This is in agreement with De Lucia et al. (2004, 2007) and Rudnick et al. (2009) who have shown the importance of lower mass (i.e., fainter) galaxies to the evolution of the color−magnitude relation and of the luminosity function versus redshift. Another interesting result has come from attempts to disentangle age, morphology and environment in the Abell 901/902 supercluster (Wolf et al. 2007; Lane et al. 2007). Local environment appears to be more important to galaxy morphology than global cluster properties, and while the expected morphology-density and age-morphology relations have been observed, there is no evidence for a morphology-density relation at a fixed age. The time since infall within the cluster environment and not density might thus be the more fundamental parameter dictating the morphology of cluster galaxies.

A number of efforts have been made on the theoretical side to model the morphological content of clusters. Diaferio et al. (2001) used a model in which the morphologies of cluster galaxies are solely determined by their merger histories. A merger between two similar mass galaxies produces a bulge, and a new disk may form through the subsequent cooling of gas. Bulge-dominated galaxies are in fact formed by mergers in smaller groups that are later accreted by clusters. Based on their model, they reach the following conclusions: (1) the fraction of bulge-dominated galaxies inside the virial radius should depend on the mass of the cluster, and it should show a pronounced peak for clusters with mass of $3 \times 10^{14}\ M_{\odot}$ followed by a decline for larger cluster masses. (2) The fraction of bulge-dominated galaxies should be independent of redshift for clusters of fixed mass; and (3) the dependence of morphology on cluster mass should be stronger at high redshift than at low redshift. Lanzoni et al. (2005) use the GALICS semi-analytical models and find that early-type fractions strongly depend on galaxy luminosity rather than cluster mass. By selecting a brighter subsample of galaxies from their simulations, they find a higher fraction of ellipticals irrespective of the cluster mass in which these galaxies reside. This trend is particularly noticeable in their high-density environments. Observations and these earlier models clearly do not agree in important areas, and a comparison between them would clearly benefit from a larger cluster sample size. More recently, the Millennium Simulation (MS; Springel et al. 2005) has provided the highest resolution model thus far of a large (0.125 Gpc$^3$), representative volume of the Universe. Improved tracking of dark matter structure and new semi-analytical prescriptions (De Lucia & Blaizot 2007) allow the evolution of the galaxy population to be followed with higher fidelity and better statistics than in the otherwise similar work of Diaferio et al. (2001). We will use cluster catalogues from the MS later in this paper for comparison with our observational data.

Our understanding of high-redshift cluster galaxy populations in terms of their evolution as a function of redshift and their cluster-to-cluster variations has been hampered by the lack of comprehensive multi-wavelength (optical, near-infrared and X-ray) imaging and spectroscopic studies of large, homogeneously-selected samples of clusters. Many efforts are underway to improve sample sizes (Gonzalez et al. 2001; Gladders & Yee 2005; Willis et al. 2005; Postman et al. 2005). One of these efforts is the European Southern Observatory Distant Cluster Survey ("EDisCS"; White et al. 2005). The

EDisCS survey is an ESO large programme aimed at the study of a sample of eighteen optically-selected clusters over the redshift range 0.5−0.8. It makes use of the FORS2 spectrograph on the Very Large Telescope for optical imaging and spectroscopy and of the SOFI imaging spectrograph on the New Technology Telescope (NTT) for near-infrared imaging. A number of papers on star formation in clusters (Poggianti et al. 2006, 2009a) and the assembly of the cluster red sequence (De Lucia et al. 2004, 2007; Sánchez-Blázquez et al. 2009; Rudnick et al. 2009) have been so far published from these data. In addition to the core VLT/NTT observations, a wealth of ancillary data are also being collected. A 80-orbit program for the Advanced Camera for Surveys (ACS) on the Hubble Space Telescope was devoted to the *i*-band imaging of our ten highest-redshift clusters. Details of the HST/ACS observations and visual galaxy classifications are given in Desai et al. (2007) and the frequency and properties of galaxy bars is studied in Barazza et al. (2009). X-ray observations with the XMM-Newton satellite of three EDisCS clusters have been published in Johnson et al. (2006) with more clusters being observed. H-alpha observations of three clusters have been published in Finn et al. (2005) with more clusters also being observed. Finally, the analysis of Spitzer/IRAC observations of all EDisCS clusters is in progress (Finn et al., in preparation).

This paper presents the early-type galaxy fractions of EDisCS clusters as a function of cluster velocity dispersion, redshift and star-formation activity. A set of local clusters extracted from the Sloan Digital Sky Survey (SDSS) is used as a comparison sample. Early-type fractions were measured from two-dimensional bulge+disk decompositions on deep, optical VLT/FORS2 and HST/ACS images of spectroscopically-confirmed cluster member galaxies. Section 2 describes the EDisCS cluster sample selection and the imaging data. Section 3 describes the procedure used to perform bulge+disk decompositions on SDSS, VLT/FORS2 and HST/ACS images. Section 4 presents early-type fractions for the EDisCS clusters with a detailed comparison between visual and quantitative morphologies and between HST- and VLT-derived early-type fractions. It also includes early-type fractions for the SDSS clusters. Changes in EDisCS early-type fractions as a function of cluster velocity dispersion, redshift and star-formation activity are studied in Sect. 5. Finally, Sects. 6 and 7 discuss our results and their implications for the morphological content of clusters. The set of cosmological parameters used throughout this paper is $(H_0, \Omega_m, \Omega_\Lambda) = (70, 0.3, 0.7)$.

## 2. Data

### 2.1. Sample selection and VLT/FORS2 optical imaging

The sample selection and optical/near-infrared imaging data for the EDisCS survey are described in details in Gonzalez et al. (2002), White et al. (2005) (optical photometry) and Aragón-Salamanca et al. (near-IR photometry, in preparation). Photometric redshifts for the EDisCS clusters are presented in Pelló et al. (2009), and cluster velocity dispersions measured from weak-lensing mass reconstructions are given in Clowe et al. (2006). Spectroscopy for the EDisCS clusters is detailed in Halliday et al. (2004) and Milvang-Jensen et al. (2008). Clusters in the EDisCS sample were drawn from the Las Campanas Distant Cluster Survey (LCDCS) candidate catalog (Gonzalez et al. 2001). Candidate selection was constrained by published LCDCS redshift and surface brightness estimates. Candidates were selected to be among the highest surface brightness detections at each redshift in an attempt to recover some of the most massive clusters at each epoch. Using the estimated contamination rate for the LCDCS of ∼30%, we targeted thirty candidates in the redshift range 0.5−0.8 for snapshot VLT/FORS2 imaging in an effort to obtain twenty (10 at $z \sim 0.5$ and 10 at $z \sim 0.8$) confirmed clusters.

The $z \sim 0.5$ candidates were observed for 20 min in each of $I_B$ and $V_B$, and the $z \sim 0.8$ candidates were observed for 20 min in each of $I_B$ and $R_{sp}$. These filters are the standard FORS2 ones. $V_B$ and $I_B$ are close approximations to the Bessell (1990) photometric system while the $R_{sp}$ is a special filter for FORS2. Final cluster candidates for deeper VLT imaging were selected on the basis of color and surface density of galaxies on the sky (White et al. 2005). The image quality on the final stacked images ranged from 0.″4 to 0.″8. As described in White et al. (2005), deep spectroscopy was not obtained for two cluster candidates (1122.9-1136 and 1238.5-1144), and we therefore did not include them here. The main characteristics (positions, redshifts, velocity dispersions and radii) of the EDisCS cluster sample used in this paper are given in Table 1. $R_{200}$ is the projected radius delimiting a sphere with interior mean density 200 times the critical density at the cluster redshift, and it is used throughout this paper as an important fiducial radius. $R_{200}$ values in Table 1 were calculated using the equation:

$$R_{200} = 1.73 \frac{\sigma}{1000\ \mathrm{km\ s^{-1}}} \frac{1}{\sqrt{\Omega_\Lambda + \Omega_m (1+z)^3}}\ h_{100}^{-1}\ \mathrm{Mpc} \quad (1)$$

where $h_{100} = H_0/100$ and $\sigma_{cluster}$ is the cluster velocity dispersion measured using spectroscopically-confirmed cluster members (Carlberg et al. 1997; Finn et al. 2005). Cluster masses were calculated using the equation:

$$M_{cl} = 1.2 \times 10^{15} \left( \frac{\sigma}{1000\ \mathrm{km\ s^{-1}}} \right)^3 \frac{1}{\sqrt{\Omega_\Lambda + \Omega_m (1+z)^3}}\ h_{100}^{-1}\ M_\odot \quad (2)$$

as in Finn et al. (2005).

In practice, the redshift distributions of high-$z$ and the mid-$z$ samples partly overlap as can be seen from Table 1.

### 2.2. VLT spectroscopy and cluster membership

We use only spectroscopically-confirmed cluster members to calculate our cluster early-type fractions. Deep multislit spectroscopy of the EDisCS was obtained with the FORS2 spectrograph on VLT. Spectra of >100 galaxies per cluster field were obtained with typical exposure times of two and four hours for the mid-$z$ and high-$z$ samples respectively. Spectroscopic targets were selected from *I*-band catalogues. This corresponds to rest-frame ∼5000 ± 400 Å at the redshifts of the EDisCS clusters. Conservative rejection criteria based on photometric redshifts were used in the selection of spectroscopic targets to reject a significant fraction of non-members while retaining a spectroscopic sample of cluster galaxies equivalent to a purely *I*-band selected one. We verified a posteriori that these criteria excluded at most 1% of the cluster galaxies (Halliday et al. 2004; Milvang-Jensen et al. 2008). The spectroscopic selection, observations and spectroscopic catalogs are presented in detail in Halliday et al. (2004) and Milvang-Jensen et al. (2008). As described in Halliday et al. (2004), cluster redshifts and velocity dispersions were iteratively calculated using a biweight scale estimator for robustness. Cluster members were defined as galaxies with redshifts within the range $z_{cluster} \pm 3\sigma_{cluster}$ where $z_{cluster}$ is the median redshift of all cluster members.

**Table 1.** Main characteristics of the EDisCS cluster sample.

| Mid-$z$ clusters ID[a] | RA[b] (2000.0) | Dec[b] (2000.0) | $z$[c] | Age of universe ($\times t_0$) | $N_{\rm mem}$[d] | $\sigma$[e] (km s$^{-1}$) | $R_{200}$[f] (Mpc) | $M_{\rm cl}$[g] ($10^{15}$ $M_\odot$) |
|---|---|---|---|---|---|---|---|---|
| (1) | (2) | (3) | (4) | (5) | (6) | (7) | (8) | (9) |
| 1018.8-1211 | 10:18:46.8 | −12:11:53 | 0.4716 | 0.654 | 33 | $474^{+75}_{-57}$ | 0.91 | 0.142 |
| 1059.1-1253 | 10:59:07.1 | −12:53:15 | 0.4550 | 0.663 | 41 | $517^{+71}_{-40}$ | 1.00 | 0.186 |
| 1119.3-1130 | 11:19:16.7 | −11:30:29 | 0.5491 | 0.615 | 21 | $165^{+34}_{-19}$ | 0.30 | 0.006 |
| 1202.7-1224 | 12:02:43.4 | −12:24:30 | 0.4246 | 0.680 | 21 | $540^{+139}_{-83}$ | 1.07 | 0.216 |
| 1232.5-1250[h] | 12:32:30.5 | −12:50:36 | 0.5419 | 0.618 | 54 | $1080^{+119}_{-89}$ | 1.99 | 1.610 |
| 1301.7-1139 | 13:01:40.1 | −11:39:23 | 0.4828 | 0.648 | 37 | $681^{+86}_{-86}$ | 1.30 | 0.418 |
| 1353.0-1137 | 13:53:01.7 | −11:37:28 | 0.5889 | 0.596 | 22 | $663^{+179}_{-91}$ | 1.19 | 0.362 |
| 1411.1-1148 | 14:11:04.6 | −11:48:29 | 0.5200 | 0.629 | 26 | $709^{+180}_{-105}$ | 1.32 | 0.461 |
| 1420.3-1236 | 14:20:20.0 | −12:36:30 | 0.4969 | 0.641 | 27 | $225^{+77}_{-62}$ | 0.43 | 0.015 |
| High-$z$ clusters ID | RA (2000.0) | Dec (2000.0) | $z$ | Age of universe ($\times t_0$) | $N_{\rm mem}$ | $\sigma$ (km s$^{-1}$) | $R_{200}$ (Mpc) | $M_{\rm cl}$ ($10^{15}$ $M_\odot$) |
| (1) | (2) | (3) | (4) | (5) | (6) | (7) | (8) | (9) |
| 1037.9-1243[h] | 10:37:51.2 | −12:43:27 | 0.5800 | 0.600 | 19 | $315^{+76}_{-37}$ | 0.57 | 0.039 |
| 1040.7-1156[h] | 10:40:40.4 | −11:56:04 | 0.7020 | 0.548 | 30 | $418^{+55}_{-46}$ | 0.70 | 0.085 |
| 1054.4-1146[h] | 10:54:24.5 | −11:46:20 | 0.6965 | 0.550 | 49 | $589^{+78}_{-70}$ | 0.99 | 0.238 |
| 1054.7-1245[h] | 10:54:43.6 | −12:45:52 | 0.7503 | 0.529 | 36 | $504^{+113}_{-65}$ | 0.82 | 0.144 |
| 1103.7-1245b[h] | 11:03:36.5 | −12:44:22 | 0.7029 | 0.548 | 11 | $242^{+126}_{-104}$ | 0.40 | 0.016 |
| 1138.2-1133[h] | 11:38:10.3 | −11:33:38 | 0.4801 | 0.649 | 48 | $737^{+77}_{-56}$ | 1.41 | 0.531 |
| 1216.8-1201[h] | 12:16:45.1 | −12:01:18 | 0.7955 | 0.513 | 67 | $1018^{+73}_{-77}$ | 1.61 | 1.159 |
| 1227.9-1138[h] | 12:27:58.9 | −11:35:13 | 0.6375 | 0.575 | 22 | $572^{+96}_{-54}$ | 0.99 | 0.226 |
| 1354.2-1231[h] | 13:54:09.7 | −12:31:01 | 0.7562 | 0.527 | 21 | $668^{+161}_{-80}$ | 1.08 | 0.335 |

[a] Clusters with HST imaging are identified by the superscript "h" in their ID; [b] cluster BCG Coordinates (J2000); [c] cluster redshift measured from EDisCS spectroscopy; [d] number of cluster members confirmed by EDisCS spectroscopy; [e] cluster velocity dispersion measured from EDisCS spectroscopy; [f] from Eq. (1); [g] from Eq. (2).

### 2.3. HST/ACS imaging

In addition to our ground-based imaging, a 80-orbit program (GO 9476, PI: Dalcanton) for the Advanced Camera for Surveys (ACS) on the Hubble Space Telescope (HST) was devoted to the $i$-band imaging of our ten highest-redshift cluster fields. Details of these observations are given in Desai et al. (2007). Briefly, the HST observations were designed to coincide as closely as possible with the coverage of the ground-based optical imaging and spectroscopy, within guide star constraints. The VLT/FORS2 images cover a $6\farcm5 \times 6\farcm5$ region around each cluster, with the cluster center displaced by $1'$ from the center of the region. For reference, the ACS WFC has a field of view of roughly $3\farcm5 \times 3\farcm5$. Balancing scientific motives for going deep over the entire spectroscopic field against a limited number of available orbits, we tiled each $6\farcm5 \times 6\farcm5$ field in four 1-orbit pointings overlapping one additional deep 4-orbit pointing on the cluster center. The resulting exposure time per pixel was 2040 s except for the central $3\farcm5 \times 3\farcm5$, which had an exposure time per pixel of 10 200 s. The deep central pointing probes to lower surface brightness, fainter magnitudes, and larger galactic radii in the region of the cluster containing the most galaxies. All exposures were taken under LOW SKY conditions to maximize our surface brightness sensitivity. An image mosaic was created for each cluster using the CALACS/Multidrizzle pipeline, and the final sampling of the multidrizzled image mosaics was $0\farcs045$. This is the "native" ACS image sampling, and it was chosen to avoid potential aliasing problems that might have been introduced by a finer multidrizzle sampling given our limited dither pattern in the cluster outskirts. Clusters with HST imaging are identified by a "h" in Table 1.

## 3. Quantitative galaxy morphology

### 3.1. Source detection and extraction

The source catalogs and segmentation images for the EDisCS clusters were created using the SExtractor ("Source Extractor") galaxy photometry package version 2.2.2 (Bertin & Arnouts 1996). The SExtractor source detection was run on the combined deep FORS2 images in "two-image" mode using the $I$-band image as the reference detection image for all the other passbands. The detection threshold was $1.5\sigma_{\rm bkg}$, and the required minimum object area above that threshold was 4 pixels. The convolution kernel was a $7 \times 7$ Gaussian kernel with a $FWHM$ of 3.0 pixels. No star/galaxy separation based on the SExtractor "stellarity" index was attempted. Every source was fit with a bulge+disk model, and unresolved sources such as stars could easily be identified as output models with zero half-light radius.

As SExtractor performs source detection and photometry, it is able to deblend sources using flux multi-thresholding. This deblending technique works well in the presence of saddle points in the light profiles between objects. Each SExtractor

pre-deblending "object" consists of all the pixels above the detection threshold that are spatially connected to one another. This group of pixels may or may not include several real objects. The multi-thresholding algorithm assigns the pixels between two adjacent objects and below the separation threshold based on a probability calculated from bivariate Gaussian fits to the two objects. No assumption is made regarding the shape of the objects in this statistical deblending technique. We used a value for the SExtractor deblending parameter DEBLEND_MINCONT of 0.0005. This value is *subjective*, and it was found through visual inspection of several EDisCS cluster images to provide good object separation. Even though the value of DEBLEND_MINCONT was determined subjectively, it provides an unequivocal definition of an object in the EDisCS catalogs. It was only determined once, and the same value of DEBLEND_MINCONT was consistently used for all EDisCS cluster images as well as for all the reliability tests of Sect. 3.2.5.

### 3.2. Two-dimensional bulge+disk decompositions

This work uses GIM2D (Galaxy IMage 2D) version 3.2, a 2D decomposition fitting program (Simard et al. 2002), to measure the structural parameters of galaxies on the EDisCS VLT/FORS2 and HST/ACS images. GIM2D is an IRAF[1]/SPP package written to perform detailed bulge+disk surface brightness profile decompositions of low signal-to-noise (S/N) images of distant galaxies in a fully automated way. GIM2D is publicly available, and it has been used extensively in a wide range of different projects so far.

#### 3.2.1. Fitting model

The fitting model used for the two-dimensional bulge+disk decompositions of EDisCS galaxies is the same as the one used by Simard et al. (2002). It consists of a "bulge" component with a de Vaucouleurs profile and of an exponential "disk" component. We put "bulge" and "disk" between quotes to emphasize that this conventional nomenclature does does not say anything about the internal kinematics of the components. The presence of a "disk" component does not necessarily imply the presence of an actual disk because many dynamically hot systems also have simple exponential profiles. The fitting model had ten free parameters: the total galaxy flux $F$, the bulge fraction $B/T$ ($\equiv$0 for pure disk systems), the bulge semi-major axis effective radius $r_e$, the bulge ellipticity $e$ ($e \equiv 1 - b/a$, $b \equiv$ semi-minor axis, $a \equiv$ semi-major axis), the bulge position angle of the major axis $\phi_b$ on the image (clockwise, $y$-axis $\equiv$ 0), the disk semi-major axis exponential scale length $r_d$ (also denoted $h$ in the literature), the disk inclination $i$ (face-on $\equiv$ 0), the disk position angle $\phi_d$ on the image, the subpixel d$x$ and d$y$ offsets of the model center with respect to the input science image center. The sky background is not a free parameter of the fits (see Sect. 3.2.3). The Sérsic index for the bulge profile is fixed at a value of $n = 4$ (i.e., the de Vaucouleurs profile value). The position angles $\phi_b$ and $\phi_d$ were not forced to be equal for two reasons: (1) a large difference between these position angles is a signature of strongly barred galaxies; and (2) some observed galaxies do have bona fide bulges that are not quite aligned with the disk position angle.

[1] IRAF is distributed by the National Optical Astronomy Observatories, which are operated by the Association of Universities for Research in Astronomy, Inc., under cooperative agreement with the National Science Foundation.

The smooth bulge+disk model used here is obviously a simple approximation. After all, many real galaxies will exhibit more than two structural components such as nuclear sources, bars, spiral arms and HII regions. Even in the presence of only a bulge and a disk, the ellipticity and/or the position angles of these components might be functions of galactocentric distance. The bulge+disk model is a trade-off between a reasonable number of fitting parameters and a meaningful decomposition of distant galaxy images. *No* non-parametric or parametric quantitative classification system is perfect. Any classification system will suffer from biases inherent to its basic definition. However, provided a given quantitative system is clearly defined before its use, its results will be readily reproducible in their successes *and* failure by other investigators.

The exact shape of bulge profiles remains under debate (e.g., Balcells et al. 2003, and references therein). Locally, there is evidence that the bulges of late-type spiral galaxies may be better fit by an $n = 1$ profile, whereas bright ellipticals and the bulges of early-type spiral galaxies follow an $n = 4$ profile (de Jong 1996; Courteau et al. 1996; Andredakis 1998). Local late-type galaxies with $n = 1$ bulges have $B/T \leq 0.1$ (de Jong 1996). Since such bulges contain only 10% of the total galaxy light, low signal-to-noise measurements of late-type high-redshift galaxies make it very difficult, if not impossible, to determine the Sérsic index of distant bulges even with the spatial resolution of the Hubble Space Telescope as demonstrated by an extensive set of tests on HST images of the high-redshift cluster CL1358+62 (Tran et al. 2003). On the other hand, $n$ is more important for bulge-dominated galaxies, and $n = 4$ is the expected value based on local early-type galaxies. Knowing that bright ellipticals and the bulges of early-type spirals are well-fit by a de Vaucouleurs profile, a $n = 4$ bulge profile was therefore adopted as the canonical bulge fitting model here for the sake of continuity across the full range of morphological types.

#### 3.2.2. Fitting regions

GIM2D disk+bulge decompositions are performed on thumbnail (or "postage stamp") images extracted around the objects detected by SExtractor rather than on the entire science image itself. The area of the thumbnail images is given by the isophotal area of the object. Here, all thumbnails were chosen to have an area 5 times larger than the $1.5\sigma_{bkg}$ isophotal area. Each thumbnail is a square image with sides of length $\sqrt{5 \times isophotal\_area}$. The first thumbnail is extracted from the science image itself, and the local background calculated by SExtractor is subtracted from it so that it should have a background mean level close to zero. The second thumbnail is extracted from the SExtractor segmentation image. The GIM2D decompositions were performed on all pixels flagged as object *or* background in the SExtractor segmentation image. Object areas in the segmentation image are sharply delineated by the location of the isophote corresponding to the detection threshold because SExtractor considers all pixels below this threshold to be background pixels. However, precious information on the outer parts of the galaxy profile may be contained in the pixels below that threshold, and fits should therefore not be restricted only to object pixels to avoid throwing that information away. Pixels belonging to objects in the neighborhood of the primary object being fit are masked out of the fitting area using the SExtractor segmentation image. The flux from the primary object that would have been in those masked areas in the absence of neighbors is nonetheless properly included in the magnitude measurements given in this paper because

magnitudes were obtained by integrating the best-fit models over *all* pixels.

#### 3.2.3. Sky background level measurements

Special care must be paid to the determination of the local sky background level $b$ and dispersion $\sigma_{\rm bkg}$ as sky errors are the dominant source of systematic errors in bulge+disk decompositions of distant galaxies. As an example, overestimating the background sky level will lead to underestimates of the galaxy total flux, half-light radius and bulge fraction as a result of strong parameter covariances. Even though the SExtractor local background was subtracted from each galaxy thumbnail image, an additional (residual) background estimate d$b$ was computed and used by GIM2D to correct for any systematic error in the initial SExtractor sky level estimate. In order to compute d$b$, GIM2D used all the pixels in the science thumbnail image flagged as background pixels (flag value of zero) in the SExtractor segmentation image. GIM2D further pruned this sample of background pixels by excluding any background pixel that is closer than five pixels (1.″0 for the pixel sampling of the FORS2 detectors) from any (primary or neighboring) object pixels. This buffer zone ensures that the flux from all SExtracted objects in the image below all the $1.5\sigma_{\rm bkg}$ isophotes does not significantly bias the mean background level upwards and artificially inflate $\sigma_{\rm bkg}$. A minimum of 7500 sky pixels was imposed on the area of the sky region. In cases where the number of sky pixels in the input science thumbnail image was insufficient, the original science image was searched for the 7500 sky pixels nearest to the object. For the EDisCS fits, background parameters were re-calculated with GIM2D before fitting, and the residual background levels d$b$ were then frozen to their recalculated values for the bulge+disk fits.

#### 3.2.4. Point-spread-functions

The shape of the point-spread-function (PSF) on the VLT/FORS2 and HST/ACS images varies significantly as a function of position, and these variations must be taken into account when point-spread-functions for the bulge+disk decompositions are generated. For both sets of images, we used the stand-alone version of the stellar photometry program DAOPHOT II (Stetson 1987) to construct spatially-varying PSF models for the EDisCS cluster images. For each cluster and for each passband, we selected "clean", point sources (detection flag of zero and stellarity index of 0.8 or greater) from the SExtractor source catalog. The positions of these point sources were fed to the DAOPHOT routine PSF to be modelled as the sum of a Gaussian core and of an empirical look-up table representing corrections from the best-fitting Gaussian to the actual observed values. Both the Gaussian core parameters and the look-up table were allowed to vary linearly as a function of $x$ and $y$ positions on the image. Finally, the PSF model was used to create a PSF at the position of each galaxy to be fit. The PSF images were 2.″5 on a side to provide good dynamical range for the fits.

#### 3.2.5. Reliability tests

Following the same procedure as in Simard et al. (2002), we performed an extensive set of simulations to test the reliability of our sky background estimates and of the best-fit parameter values recovered through bulge+disk fits on both sets of images. 2000 smooth galaxy image models were created with structural parameters uniformly generated at random in the following ranges: $20.0 \leq I \leq 25.0$, $0.0 \leq B/T \leq 1.0$, $0 \leq r_{\rm e} \leq 10.''0$, $0.0 \leq e \leq 0.7$, $0 \leq r_{\rm d} \leq 10.''0$, and $0^\circ \leq i \leq 85^\circ$. The bulge Sérsic index was held fixed at $n = 4$ for all models. Both bulge and disk position angles were fixed to 90° for all simulations, and the bulge and disk sizes were uniformly generated in the log of the size ranges above. Each simulation was convolved with a PSF computed from one of the images with a *FWHM* typical of the VLT/FORS2 (~0.″8) and HST/ACS (~0.″05) observations. The same PSF was used in both creating and analyzing the simulations, so the results will not include any error in the structural parameters due to PSF mismatch. Poisson deviates were used to add photon noise due to galaxy flux into the simulations. The noisy images were then embedded in a $20'' \times 20''$ section of one of the real $I$-band images to provide a real background for the simulations. In addition to sky photon noise and detector readout noise, the real background noise includes brightness fluctuations of very faint galaxies below the detection threshold. This procedure thus yields realistic errors that include the effect of sky errors. The simulations were SExtracted exactly in the same way as real EDisCS sources (see Sect. 3.1). Science and segmentation thumbnails extracted from the simulations were analyzed with GIM2D following exactly the same steps as for the real galaxies (see Sect. 3.2).

Figures 1 and 2 show maps of errors on the galaxy total magnitude $I$, galaxy intrinsic half-light radius $r_{\rm hl}$ and galaxy bulge fraction $B/T$ for the VLT/FORS2 images. The left-hand panels show the mean parameter errors as a function of input galaxy magnitude and size, and the right-hand panels show the $1\sigma$ parameter random error as a function of input galaxy magnitude and size. The lower number in each cell is the number of simulated galaxies created for that cell. Most systematic errors are directly related to surface brightness as magnitudes and sizes of low surface brightness sources are inherently harder to measure. This fact is borne out by the trends in the errors shown in Fig. 1. Decreasing surface brightness follows a line going from the lower left-hand corners to the upper right-hand ones. The top panels of Figs. 1 show that systematic errors on $I$ start to become significant ($\Delta I \simeq 0.2$) fainter than $I = 22.5$. Systematic errors on $\log r_{\rm hl}$ also increases significantly beyond this magnitude. It is important to note that $I = 22.5$ is significantly fainter by about 2 mag than the galaxies that will be used to compute cluster early-type galaxy fractions in Sect. 4.3, so these galaxy fractions should be unaffected. Figure 2 shows that systematic errors on $B/T$ are smallest over the region $I \leq 22.5, -0.5 \leq \log r_{\rm hl} \leq 0.3$ where most of the real EDisCS galaxies actually lie. As mentioned above, our reliability tests do not include the effects of PSF mismatch errors because we used the same PSF for creating simulated images and for their analysis. However, we were able to check that these errors were not significant because we fitted both galaxies *and* stars on our real VLT/FORS2 images. The measured intrinsic radii of the stars clustered at zero, and this would not have been the case should PSF mismatch errors have been important.

## 4. Early-type galaxy fractions

### 4.1. Definition and comparison with galaxy visual classifications

The bulk of the previous work on the morphological content of high-redshift clusters is based on the visual classification of galaxies, and this section compares visual and quantitative morphological classification. Visual classifications for 9200 galaxies

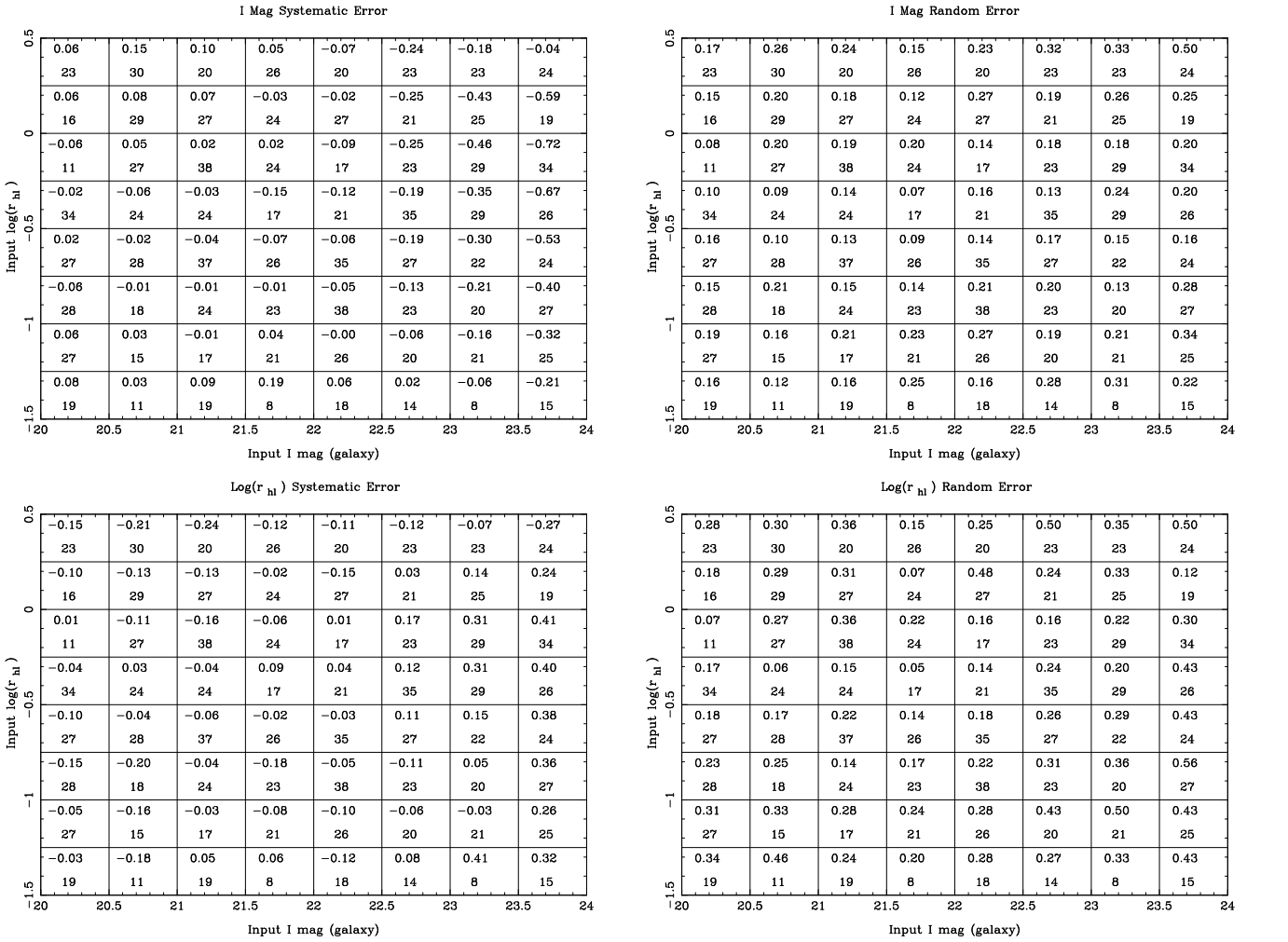


**Fig. 1.** Two-dimensional maps of GIM2D systematic and random galaxy magnitude and half-light radius errors from 2000 VLT/FORS2 image simulations. *Top left-hand panel*: systematic error on recovered galaxy total magnitude $I_{\rm rec}$ as a function of *input* galaxy log half-light radius $r_{\rm hl,input}$ in arcseconds and *input* galaxy total magnitude $I_{\rm input}$. The top number in each cell is the mean magnitude error ($I_{\rm rec} - I_{\rm input}$), and the bottom number is the number of simulations created in that cell. *Top right-hand panel*: $1\sigma$ random error on $I_{\rm rec}$ ($\sigma(I_{\rm rec} - I_{\rm input})$) as a function of log $r_{\rm hl,input}$ and $I_{\rm input}$. *Bottom left-hand panel*: systematic error on recovered galaxy intrinsic log half-light radius $r_{\rm hl,rec}$ as a function of *input* galaxy log half-light radius $r_{\rm hl,input}$ in arcseconds and *input* galaxy total magnitude $I_{\rm input}$. The top number in each cell is the mean log radius error (log $r_{\rm hl,rec}$ − log $r_{\rm hl,input}$), and the bottom number is the number of simulations created in that cell. *Top right-hand panel*: $1\sigma$ random error on log $r_{\rm hl,rec}$ ($\sigma$(log $r_{\rm hl,rec}$ − log $r_{\rm hl,input}$)) as a function of log $r_{\rm hl,input}$ and $I_{\rm input}$.

in EDisCS clusters with HST images are presented in Desai et al. (2007). As shown by previous works (Im et al. 2002; McIntosh et al. 2002; Tran et al. 2003; Blakeslee et al. 2006), quantitative and visual morphologies can be best linked together by focussing on three structural parameters: bulge fraction $B/T$, image smoothness $S$ and bulge ellipticity $e$. The image smoothness, $S$, is defined as:

$$S = R_T + R_A \tag{3}$$

where $R_T$ and $R_A$ are defined in Eq. (11) of Simard et al. (2002). These two indices quantify the amount of light in symmetric and asymmetric residuals from the fitting model respectively, and they are expressed as a fraction of the total galaxy model flux. $S$ is typically measured inside a radius that is a multiple of the galaxy half-light radius. Using our HST/ACS measurements, we found no differences between image smoothness within one and two galaxy half-light radii. We therefore use image smoothness inside two half-light radii (and denote it $S2$ hereafter) because it is more reliably measured on the VLT/FORS2 images with their lower spatial resolution. We can choose selection criteria on $B/T$, $S$ and $e$ that yield the best match to the visual classifications, and the particular choices are not important as long as the same selection criteria are applied to both local and high-redshift clusters.

We divide the visually-classified EDisCS into $T = -5$ (E), $-2$ (S0), 1 (S0/a) and "others" ($T > 1$). Using our HST/ACS structural parameter measurements, we find that E and S0 galaxies have similar $B/T$ distribution with the S0 distribution being skewed towards slightly lower $B/T$, but $e$ distributions are different. It is therefore possible to differentiate between E and S0 galaxies on the basis of these two parameters. S0 and S0/a galaxies have similar $e$ distributions but different $B/T$ and $S$ distributions. Given that the bulge ellipticity $e$ cannot be reliably measured on the VLT/FORS2 images, we restrict on selection criteria to $B/T$ and $S2$. Figure 3 shows $S2$ versus $B/T$ for the four visual types of galaxies. $S2$ can take on small negative values due to statistical background subtraction terms (Simard et al. 2002). The optimal choice of limits on $B/T$ and $S2$ for our definition of early-type fraction is driven by the need to maximize the number of E/S0 galaxies selected while minimizing

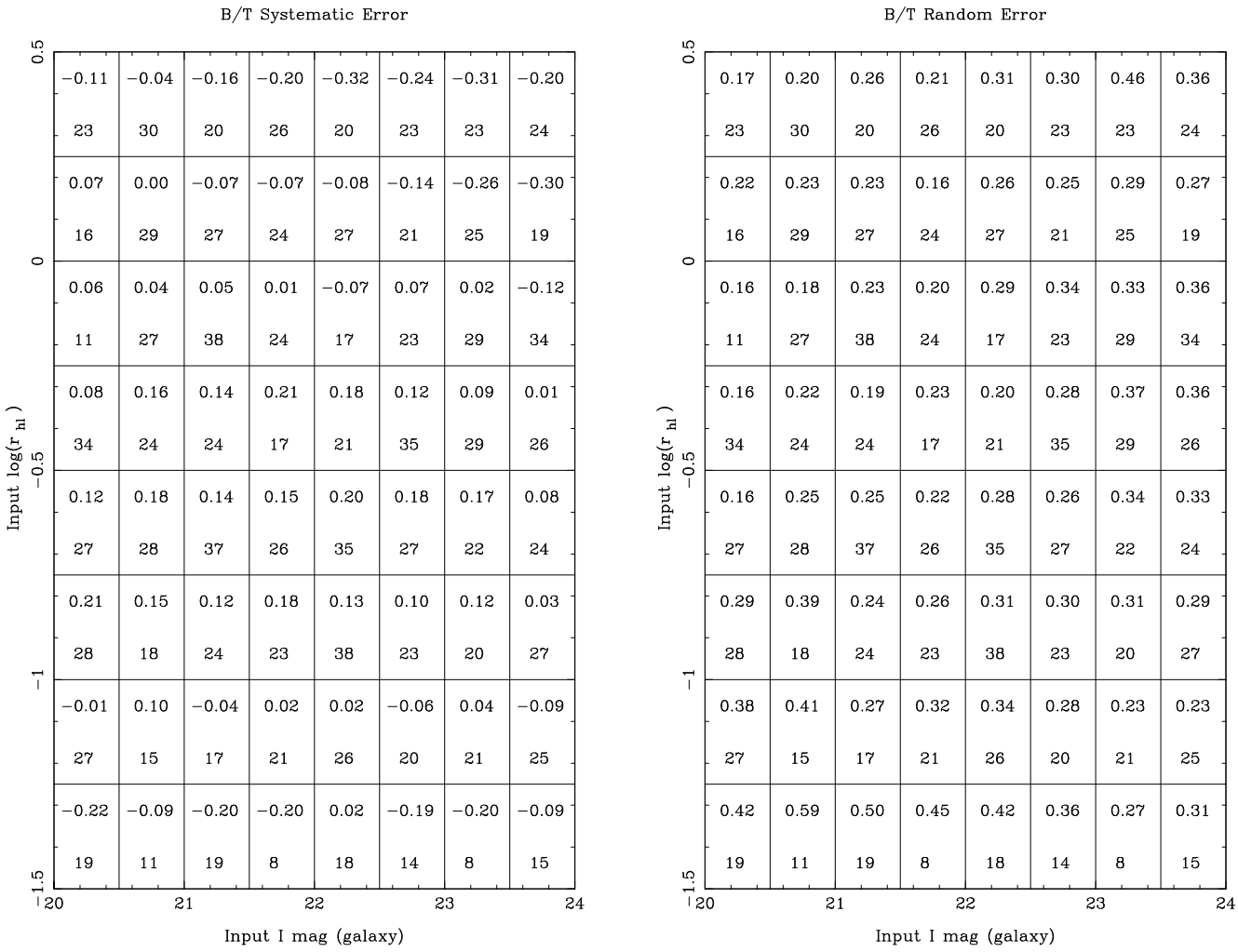


**Fig. 2.** Two-dimensional maps of GIM2D systematic and random galaxy bulge fraction errors from 2000 VLT/FORS2 image simulations. *Top left-hand panel*: systematic error on recovered galaxy bulge fraction $(B/T)_{\rm rec}$ as a function of *input* galaxy log half-light radius $r_{\rm hl,input}$ in arcseconds and *input* galaxy total magnitude $I_{\rm input}$. The top number in each cell is the mean bulge fraction error $((B/T)_{\rm rec} - (B/T)_{\rm input})$, and the bottom number is the number of simulations created in that cell. *Top right-hand panel*: $1\sigma$ random error on $(B/T)_{\rm rec}$ $(\sigma((B/T)_{\rm rec} - (B/T)_{\rm input}))$ as a function of log $r_{\rm hl,input}$ and $I_{\rm input}$.

the contamination from Sa-Irr galaxies. After several iterations, we settled on $B/T \geq 0.35$ and $S2 \leq 0.075$ as our definition of an early-type galaxy. These limits are very similar to those used in previous studies (Im et al. 2002; McIntosh et al. 2002; Tran et al. 2003). With these criteria, our quantitative selection can be translated into visual classification terms as

$$f_{\rm et} = (0.69N_{\rm E} + 0.71N_{\rm S0} + 0.35N_{\rm S0/a} + 0.04N_{\rm Sa-Irr})\,/N_{\rm total}. \quad (4)$$

The coefficients in Eq. (4) give the completeness of the quantitative classification in terms of the Desai et al. (2007) visual classes. For example, the adopted $B/T$ and $S2$ cuts would select 69% of the galaxies visually classified by Desai et al. (2007) as E's, 71% of their S0's and so on. As mentioned earlier, E's and S0's cannot be distinguished using only $B/T$ and $S2$. Equation (4) is to be compared to the prescription of van Dokkum et al. (2000):

$$f_{\rm et} = \left(N_{\rm E} + N_{\rm E/S0} + N_{\rm S0} + \frac{1}{2}N_{\rm S0/a}\right)/N_{\rm total} \quad (5)$$

where $N_{\rm total}$ is the number of galaxies with $M_V \leq -20$.

It is impossible to recover all the galaxies visually classified as early-types because a visual early-type does not necessarily imply a $r^{1/4}$ profile. Indeed, many early-type galaxies such as dwarf ellipticals have simple exponential profiles (Lin & Faber 1983; Kormendy 1985), and we have verified through isophote tracing that many galaxies visually classified as early-types and missed by our selection criteria do have radial surface brightness profiles that are exponential and thus consistent with their measured low $B/T$ values.

Given $N_{\rm total}$ galaxies brighter than an absolute magnitude limit $M_{V,\rm lim}$ inside a clustercentric radius $R_{\rm max}$ of which $N_{\rm et}$ are early-types galaxies, we actually calculate the early-type galaxy fraction by finding the median of the binomial probability distribution

$$p(x)\mathrm{d}x = \frac{N_{\rm total}!}{N_{\rm et}!(N_{\rm total} - N_{\rm et})!} x^{N_{\rm et}}(1-x)^{N_{\rm total}-N_{\rm et}} \quad (6)$$

and we integrate Eq. (6) to calculate the lower and upper bounds of the corresponding 68% confidence interval. In the limit of large $N_{\rm total}$ and $N_{\rm et}$ (not always true for the current cluster sample), this converges to the same symmetric error bars as would be obtained from the propagation of Gaussian errors.

**Table 2.** Early-type galaxy fractions based on HST/ACS imaging.

| ID | $R_{\rm et} \leq 0.6\,R_{200}$ | | | | | | $R_{\rm et} \leq R_{200}$ | | | |
|---|---|---|---|---|---|---|---|---|---|---|
| | $N_{\rm clus}$ | $N_{\rm et}$ | $f_{\rm et,raw}$ | $f_{\rm et,corr}$ | $f^{a}_{\rm E/S0,phz}$ | $f^{b}_{\rm E/S0,bkg}$ | $N_{\rm clus}$ | $N_{\rm et}$ | $f_{\rm et,raw}$ | $f_{\rm et,corr}$ |
| (1) | (2) | (3) | (4) | (5) | (6) | (7) | (8) | (9) | (10) | (11) |
| 1216.8-1201 | 45 | 23 | 0.51 ± 0.07 | 0.55 ± 0.07 | 0.47 ± 0.06 | 0.54 ± 0.06 | 57 | 25 | 0.44 ± 0.06 | 0.42 ± 0.06 |
| 1040.7-1156 | 9 | 4 | 0.45 ± 0.15 | 0.45 ± 0.15 | 0.53 ± 0.17 | 0.37 ± 0.17 | 13 | 5 | 0.40 ± 0.12 | 0.33 ± 0.12 |
| 1054.4-1146 | 18 | 9 | 0.50 ± 0.11 | 0.29 ± 0.10 | 0.28 ± 0.09 | 0.24 ± 0.09 | 26 | 11 | 0.43 ± 0.10 | 0.28 ± 0.09 |
| 1054.7-1245 | 11 | 8 | 0.70 ± 0.13 | 0.46 ± 0.14 | 0.44 ± 0.16 | 0.57 ± 0.13 | 19 | 10 | 0.52 ± 0.11 | 0.38 ± 0.11 |
| 1232.5-1250 | 48 | 28 | 0.58 ± 0.07 | 0.58 ± 0.07 | 0.60 ± 0.06 | 0.45 ± 0.06 | 51 | 28 | 0.55 ± 0.07 | 0.47 ± 0.07 |
| 1037.9-1243 | 8 | 1 | 0.18 ± 0.12 | 0.18 ± 0.12 | 0.13 ± 0.09 | 0.08 ± 0.07 | 8 | 1 | 0.18 ± 0.12 | 0.18 ± 0.12 |
| 1103.7-1245b | 2 | 0 | 0.21 ± 0.20 | 0.21 ± 0.20 | 0.47 ± 0.20 | 0.21 ± 0.20 | 4 | 0 | 0.13 ± 0.13 | 0.13 ± 0.13 |
| 1354.2-1231 | 8 | 5 | 0.61 ± 0.15 | 0.39 ± 0.15 | 0.35 ± 0.14 | 0.44 ± 0.19 | 12 | 5 | 0.42 ± 0.13 | 0.28 ± 0.11 |
| 1138.2-1133 | 22 | 4 | 0.20 ± 0.08 | 0.20 ± 0.08 | 0.37 ± 0.09 | 0.50 ± 0.14 | 24 | 6 | 0.26 ± 0.08 | 0.34 ± 0.09 |

[a] From Table 14 of Desai et al. (2007); [b] from Table 16 of Desai et al. (2007).

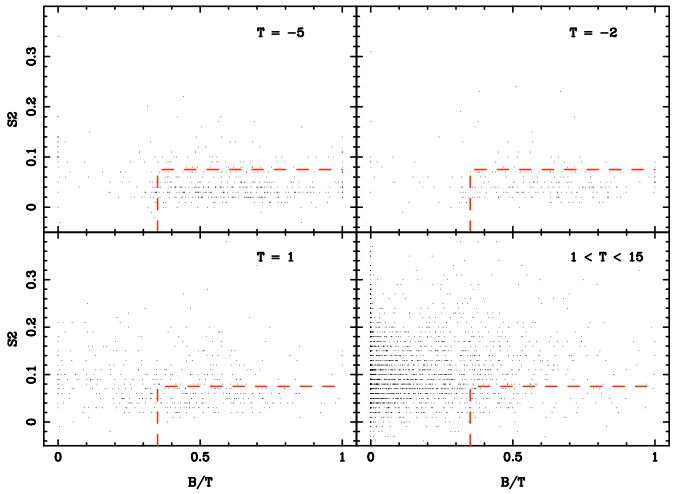


**Fig. 3.** Image smoothness parameter $S2$ versus bulge fraction $B/T$ for different visual types. The galaxies selected by our quantitative early-type galaxy criteria ($B/T \geq 0.35$ and $S2 \leq 0.075$) are enclosed in the area delimited by dashed lines.

### 4.2. HST-based fractions

For each EDisCS cluster with HST/ACS imaging, we have computed the fraction of early-type galaxies using our quantitative HST/ACS morphologies ($B/T \geq 0.35$ and and $S2 \leq 0.075$). We used only spectroscopically-confirmed members brighter than an absolute $V$-band magnitude $M_{V,\rm lim}$. We varied $M_{V,\rm lim}$ as a function of redshift from $-20.5$ at $z = 0.8$ to $-20.1$ at $z = 0.4$ to account for passive evolution. This choice of $M_{V,\rm lim}$ was made to be fully consistent with previous work (Poggianti et al. 2006) although it may not be strictly the best choice for late-type galaxy populations. Our results did not appear to be sensitive to variations in $M_{V,\rm lim}$ at the level of a few tens of a magnitude. Following Poggianti et al. (2006), our early-type galaxy fractions were also computed by weighting each galaxy according to the incompleteness of the spectroscopic catalog. This incompleteness depends on both galaxy magnitude and clustercentric position. Incompleteness as a function of magnitude was computed by dividing the number of galaxies in the spectroscopic catalog in a given magnitude bin by the number of galaxies in the parent photometric catalog in the same bin. We used 0.5 mag bins here. Incompleteness due to the geometrical effects comes from the finite number of slitlets per sky area, and the increasing surface density of galaxies on the sky closer to the cluster centers. Geometric incompleteness is field dependent as it depends on cluster richness, and we thus computed this incompleteness on a field-by-field basis. We also used four radial bins out to $R_{200}$ with a bin width of 0.25 $R_{200}$.

The raw and incompleteness-corrected HST-based early-type galaxy fractions are given in Table 2 for a maximum clustercentric radius $R_{\rm et}$ of 0.6 $R_{200}$ (Cols. 4 and 5) and $R_{200}$ (Cols. 9 and 10). Most of the corrected fractions do not significantly differ from the raw ones because our spectroscopic sample is essentially complete down to $I \leq 23$ ($M_V \sim -20$ at $z = 0.8$), and we used multiple masks on dense clusters to improve the spatial sampling of our spectroscopic sample. As a comparison, Table 2 also gives early-type galaxy fractions measured from visual classifications by Desai et al. (2007) (Cols. 6 and 7). They should be compared with values in Col. 5 because cluster galaxy samples selected using photometric redshifts are de facto free from the magnitude and geometric incompleteness of our spectroscopic sample. Another important caveat is that they were computed using two different ways to isolate cluster members (photometric redshift and statistical background subtraction), and they are thus not restricted to spectroscopically-confirmed members. Nonetheless, the agreement between fractions measured from visual and quantitative classifications is remarkably good. The largest disagreement is for 1138.2-1133, but even this case can be considered marginal as it is not quite $2\sigma$.

### 4.3. VLT- versus HST-based fractions

Quantitative morphologies measured from HST images are more robust than those measured from ground-based images (Sect. 3.2.5 and Simard et al. (2002)). Figure 4 shows a direct galaxy-by-galaxy comparison between bulge fraction and image smoothness measurements from HST/ACS and VLT/FORS2 images. This comparison includes spectroscopically-confirmed member galaxies from all clusters with HST imaging that are brighter than $M_{V,\rm lim}$ and within a clustercentric radius of 0.6 $R_{200}$ to take into account the effect of crowding. For a given galaxy, the agreement between the two sets of measurements will obviously depend on its apparent luminosity and size. The overall agreement is reasonably good. The scatter in the bulge fraction plot is consistent with $\sigma_{B/T,\rm ACS} \sim 0.1$ (Simard et al. 2002) and $\sigma_{B/T,\rm VLT} \sim 0.25$ (Fig. 2) added in quadrature, but the fact that completely independent segmentation images were used for the HST and VLT morphological measurements also contributes

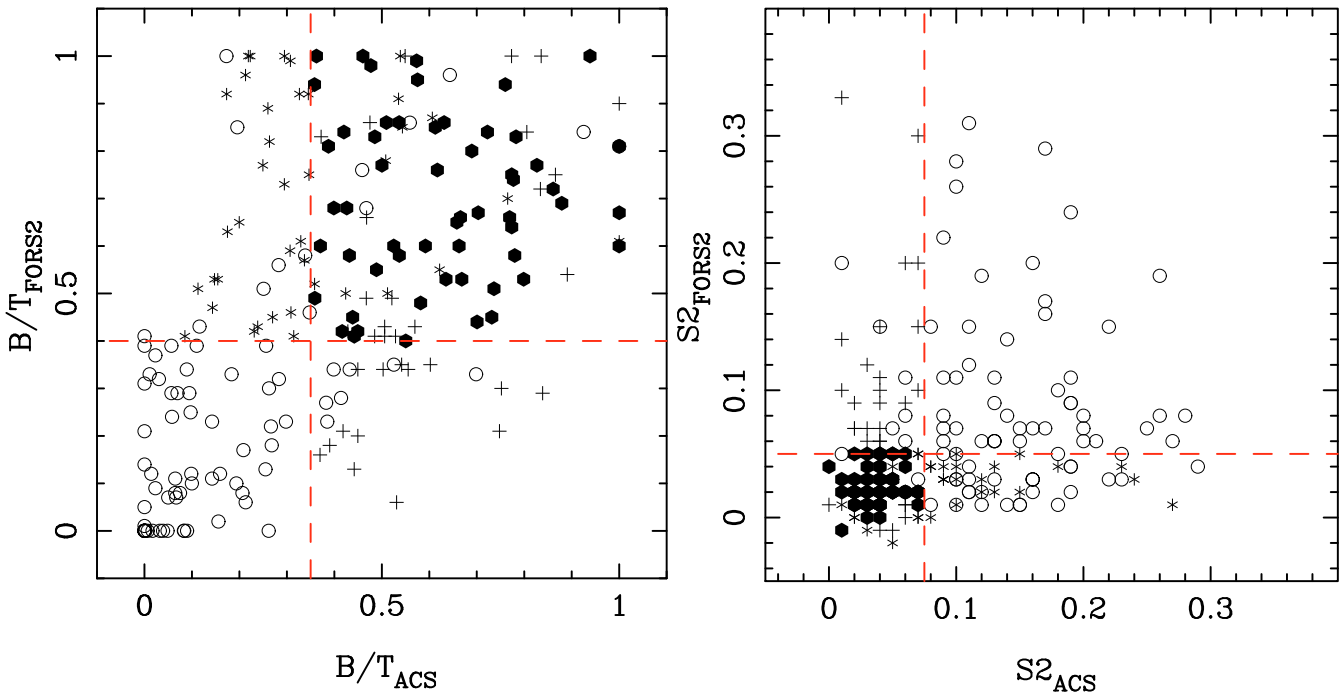


**Fig. 4.** Direct galaxy-by-galaxy comparison between bulge fraction (*left-hand panel*) and image smoothness (*right-hand panel*) measurements from HST/ACS and VLT/FORS2 images. Filled circles are galaxies classified as early-type on both ACS and VLT images, asterisks are galaxies classified as early-type only on the VLT images, pluses are galaxies classified as early-type only on the ACS images, and open circles are galaxies not classified as early-type on either ACS or VLT images, The dashed lines show the cuts used for the definition of an early-type galaxy as discussed in Sects. 4.1 and 4.3.

significantly to this scatter. Indeed, this scatter would be smaller if only uncrowded galaxies (as indicated by the SExtractor photometry flag) on the VLT images had been plotted here. For the image smoothness plot, there is a correlation between $S2_{\rm FORS2}$ and $S2_{\rm ACS}$, but it is not one-to-one. $S2_{\rm ACS}$ values increase faster than $S2_{\rm FORS2}$. This is expected as PSF blurring will be more significant on the ground-based images, and $S2$ measurements are not corrected for PSF effects. Part of the scatter is again due to the use of independent segmentation images.

The inclusion of clusters with only VLT/FORS2 imaging allows us to extend our analysis to nine additional clusters – an important consideration given that we seek to probe cluster-to-cluster variations in morphological content. We therefore need to show that we measure consistent early-type fractions for clusters with overlapping ACS and FORS2 images. The problem boils down to finding the set of limits on $B/T_{\rm FORS2}$ and $S2_{\rm FORS2}$ that yield FORS2 early-type fractions in agreement with the ACS fractions obtained with $B/T_{\rm ACS} \geq 0.35$ and $S2_{\rm ACS} \leq 0.075$ when the same galaxies are used for both FORS2 and ACS. For each cluster, we used all spectroscopically-confirmed cluster members brighter than $M_{V,\rm lim}$ and within a clustercentric radius of $R_{200}$. No corrections for incompleteness were applied here as these corrections would be identical for both cases. We went through many manual iterations until we found satisfactory limits on $B/T_{\rm FORS2}$ and $S2_{\rm FORS2}$. We found FORS2 fractions to be in very good agreement with the ACS ones for $B/T_{\rm FORS2} \geq 0.40$ and $S2_{\rm FORS2} \leq 0.05$ (Fig. 5). This agreement is especially good if one considers the fact that we performed our FORS2 and ACS bulge+disk decompositions completely independently from one another, i.e., we did not attempt to use the same SExtractor segmentation map for both FORS2 and HST images. The limit on $B/T_{\rm FORS2}$ is slightly higher than the one on $B/T_{\rm ACS}$ because lower spatial resolution typically leads to a small overestimate of the bulge fraction. Similarly, the limit on $S2_{\rm FORS2}$ needs to be more stringent than on $S2_{\rm ACS}$ to select

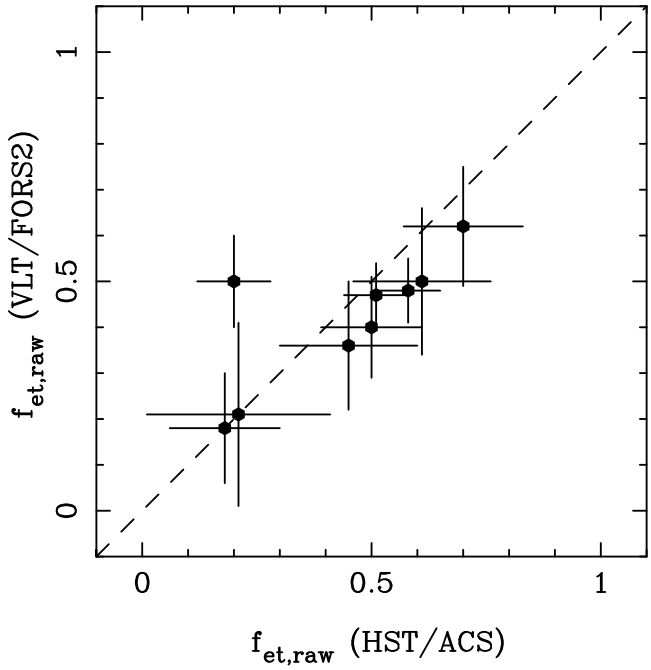


**Fig. 5.** Comparison between early-type galaxy fractions for clusters with overlapping VLT and HST imaging. VLT/FORS2 and HST/ACS early-type galaxy fractions were computed using galaxies with $B/T_{\rm FORS2} \geq 0.40$ and $S2_{\rm FORS2} \leq 0.05$ and $B/T_{\rm ACS} \geq 0.35$ and $S2_{\rm ACS} \leq 0.075$ respectively. The ACS and FORS2 $f_{\rm et}$ values plotted here are listed in Col. 4 of Table 2 and Col. 4 of Table 3. Dashed line is the one-to-one line.

**Table 3.** Early-type galaxy fractions based on VLT/FORS2 imaging.

| ID | $M_{V,\lim}$ | $R_{\rm et} \leq 0.6\,R_{200}$ | | | $R_{\rm et} \leq R_{200}$ | | |
|---|---|---|---|---|---|---|---|
| | | $N^a$ | $f_{\rm et,raw}$ | $f_{\rm et,corr}$ | $N^a$ | $f_{\rm et,raw}$ | $f_{\rm et,corr}$ |
| (1) | (2) | (3) | (4) | (5) | (6) | (7) | (8) |
| 1018.8-1211 | −20.2 | 18 | 0.60 ± 0.11 | 0.55 ± 0.11 | 20 | 0.59 ± 0.11 | 0.55 ± 0.11 |
| 1059.1-1253 | −20.2 | 20 | 0.64 ± 0.10 | 0.59 ± 0.10 | 28 | 0.64 ± 0.09 | 0.60 ± 0.09 |
| 1119.3-1130 | −20.3 | 6 | 0.64 ± 0.17 | 0.77 ± 0.15 | 9 | 0.64 ± 0.14 | 0.74 ± 0.15 |
| 1202.7-1224 | −20.1 | 11 | 0.54 ± 0.14 | 0.54 ± 0.14 | 13 | 0.60 ± 0.13 | 0.67 ± 0.13 |
| 1232.5-1250 | −20.2 | 48 | 0.48 ± 0.07 | 0.60 ± 0.07 | 51 | 0.49 ± 0.07 | 0.62 ± 0.07 |
| 1301.7-1139 | −20.2 | 17 | 0.53 ± 0.11 | 0.53 ± 0.11 | 28 | 0.43 ± 0.09 | 0.40 ± 0.09 |
| 1353.0-1137 | −20.3 | 9 | 0.55 ± 0.15 | 0.55 ± 0.15 | 17 | 0.42 ± 0.11 | 0.36 ± 0.11 |
| 1411.1-1148 | −20.2 | 15 | 0.47 ± 0.12 | 0.53 ± 0.12 | 16 | 0.44 ± 0.12 | 0.44 ± 0.11 |
| 1420.3-1236 | −20.2 | 4 | 0.50 ± 0.20 | 0.50 ± 0.20 | 7 | 0.56 ± 0.17 | 0.44 ± 0.17 |
| 1037.9-1243 | −20.3 | 8 | 0.18 ± 0.12 | 0.18 ± 0.12 | 8 | 0.18 ± 0.12 | 0.18 ± 0.12 |
| 1040.7-1156 | −20.4 | 9 | 0.36 ± 0.14 | 0.36 ± 0.14 | 13 | 0.46 ± 0.13 | 0.46 ± 0.13 |
| 1054.4-1146 | −20.4 | 18 | 0.40 ± 0.11 | 0.34 ± 0.11 | 26 | 0.39 ± 0.09 | 0.35 ± 0.09 |
| 1054.7-1245 | −20.5 | 11 | 0.62 ± 0.13 | 0.38 ± 0.13 | 19 | 0.52 ± 0.11 | 0.43 ± 0.11 |
| 1103.7-1245b | −20.4 | 2 | 0.21 ± 0.20 | 0.21 ± 0.20 | 3 | 0.39 ± 0.22 | 0.39 ± 0.22 |
| 1138.2-1133 | −20.2 | 22 | 0.50 ± 0.10 | 0.46 ± 0.10 | 24 | 0.54 ± 0.10 | 0.54 ± 0.10 |
| 1216.8-1201 | −20.5 | 45 | 0.47 ± 0.07 | 0.53 ± 0.07 | 57 | 0.46 ± 0.06 | 0.46 ± 0.06 |
| 1227.9-1138 | −20.3 | 9 | 0.26 ± 0.13 | 0.16 ± 0.11 | 11 | 0.30 ± 0.12 | 0.22 ± 0.11 |
| 1354.2-1231 | −20.5 | 8 | 0.50 ± 0.16 | 0.39 ± 0.15 | 12 | 0.35 ± 0.12 | 0.28 ± 0.11 |

[a] Number of cluster members brighter than $M_{V,\lim}$ inside $R_{\rm et}$.

the same galaxies as they will look smoother on the FORS2 images due to lower resolution.

Following the procedure described in Sect. 4.2, we computed early-type galaxy fraction for all eighteen clusters using galaxies on our FORS2 images with $B/T_{\rm FORS2} \geq 0.40$ and $S2_{\rm FORS2} \leq 0.05$. The results are shown in Table 3. The same incompleteness corrections as in Sect. 4.2 were applied here as well. The errors on the early-type galaxy fractions in the table do not include errors on $R_{200}$ due to correlated errors on cluster $\sigma$. We hereafter use our VLT/FORS2 early-type fractions for all EDisCS clusters for the sake of uniformity.

### 4.4. Local clusters

The Sloan Digital Sky Survey (SDSS; Abazajian et al. 2009) offers by far the best, "local" ($z < 0.1$) baseline for a comparison of early-type galaxy fractions between local and high-redshift clusters. Clusters similar in mass to EDisCS clusters can be selected from spectroscopic SDSS data, *and* galaxy morphologies can be measured using GIM2D from SDSS images. We therefore used SDSS-selected clusters here to construct a local baseline as nearly free of systematics as currently possible given the available data.

We use the sample of SDSS clusters defined in von der Linden (2007). The basis of this cluster sample is the C4 cluster catalogue (Miller et al. 2005), and we briefly recapitulate here how the von der Linden et al. sample was selected. Their primary aim was to find the galaxy closest to the deepest point of the potential well of a cluster. In order to insure that the clusters would span a large angular extent compared to the minimum distance of 55 arcsec between fibers, the sample was restricted to redshifts $z \leq 0.1$. This first cut resulted in an initial sample of 833 clusters. A combination of clustercentric distance, galaxy concentration and colour cuts was used to identify brightest cluster galaxies (BCGs) for these clusters. For cases where the same BCG was identified for more than one cluster, only the cluster with the density peak was retained, and the others were deemed to be substructures. This cut rejected 101 clusters. Refined velocity dispersion and virial radii were then computed through an iterative process of velocity cuts. This process failed for 55 clusters, and these were also rejected. All remaining clusters were then visually inspected. An additional set of 35 clusters were rejected at this point as being in the infall regions of other clusters, and another 17 clusters were discarded because they had less than three galaxies within $3\sigma$ of the cluster redshift and 1 $R_{200}$ of its center. This brought the total of SDSS clusters down to 625. Following Poggianti et al. (2006), we applied a final redshift cut to keep clusters in the range $0.04 < z < 0.085$. The lower limit reduces fiber aperture effects, and the upper limit minimizes incompleteness in galaxy absolute magnitude. Our final SDSS comparison sample thus has 439 clusters.

Given that we are interested in probing galaxy properties as a function of environment, it is important to ensure that the SDSS and EDisCS samples both cover the same range of environments. We therefore selected a subsample of SDSS clusters with a velocity dispersion distribution matching the EDisCS distribution. This match was done by adding SDSS clusters to the subsample one at a time and keeping only those that maintained the EDisCS-SDSS two-sample Kolmogorov-Smirnov probability above 50%. This is the probability of the maximum difference between the normalized cumulative distributions of the EDisCS and SDSS samples. It means that even if the two sampls were selected at random from the same underlying distribution, they would differ by more than the two observed samples more than half the time. This probability threshold thus yields a SDSS subsample that is very well-matched to the EDisCS clusters. The resulting subsample (referred to as "SDSS-C4" hereafter) includes 158 clusters, and these clusters are listed in Table 4.

We ran GIM2D on SDSS Data Release Seven (DR7; Abazajian et al. 2009) *u*-, *g*-, *r*- and *i*-band images of objects in the magnitude range $14 \leq r_{\rm petrosian,corr} \leq 17.77$ with a galaxy spectrum (i.e., with field SpecClass = 2 in database table SpecPhoto). Bulge+disk decompositions were successfully obtained for 674 693 galaxies (Simard, in preparation). GIM2D morphologies for galaxies in our matched SDSS-C4 clusters were extracted from this large morphological database to compute early-type fractions. There are two sources

of incompleteness that must be taken into account here. The first one is incompleteness versus magnitude. We denote this spectroscopic completeness function as $C_{\rm mag}(m)$ here, and we compute it around each cluster position by taking the ratio of the number of galaxies in the spectroscopic SDSS catalog (database table SpecPhoto) to the number of galaxies in the photometric SDSS catalog (database table PhotoPrimary) as a function of Petrosian $r$ magnitude. Galaxies around a given position on the sky were extracted from the database using the SDSS "fGetNearbyObjEq" function. The second source of incompleteness comes from the spatial sampling of the SDSS fibers on the sky. Fibers cannot be placed closer than 55″ from one another. This means that regions with a higher surface density of targets could not be sampled as completely as regions in the global field. The net result for SDSS clusters is a decrease in spectroscopic sampling as a function of decreasing clustercentric distance $R$. We can map the spectroscopic completeness versus $R$ by computing the ratio of galaxies in the spectroscopic and photometric SDSS catalogs as a function of $R$. We denote this geometrical completeness function as $C_{\rm geom}(R)$ here. Ideally, $C_{\rm geom}(R)$ should be computed for each cluster because it will depend on cluster richness and apparent size (and thus indirectly on redshift). However, in practice, there are not enough galaxies in a single cluster to yield $C_{\rm geom}(R)$ with acceptable error bars. So, we opted for averaging clusters with the same redshifts and velocity dispersions to compute $C_{\rm geom}(R)$. We divided the cluster list of Table 4 into three cluster groups: (1) $z < 0.06$; (2) $z > 0.06$, $\sigma < 800$ km s$^{-1}$; and (3) $z > 0.06$, $\sigma > 800$ km s$^{-1}$. The weight $W_{\rm spec}(m, R)$ in the spectroscopic catalog of a galaxy with a $r'$-band magnitude $m$ at a clustercentric $R$ is thus given by the product $\frac{1}{C_{\rm mag}(m)} \frac{1}{C_{\rm geom}(R)}$, and the completeness-weighted early-fraction of a SDSS cluster is then simply:

$$f_{\rm et}\left(\begin{array}{c} M_V \le -19.8, \\ B/T \ge 0.35, \\ S2 \le 0.075 \end{array}\right) = \frac{\sum\limits_{\substack{i \in [M_V \le -19.8, \\ R \le R_{\rm et}, \\ B/T \ge 0.35, \\ S2 \le 0.075]}} W_{\rm spec}(m_i, R_i)}{\sum\limits_{\substack{i \in [M_V \le -19.8, \\ R \le R_{\rm et}]}} W_{\rm spec}(m_i, R_i)}. \quad (7)$$

In terms of spatial resolution, the ACS, SDSS and FORS2 images have sampling of 0.68 kpc/*FWHM* at $z = 0.8$ (0.″09 *FWHM* in $i$), 1.87 kpc/*FWHM* at $z = 0.07$ (1.″4 *FWHM* in $g$) and 4.5 kpc/*FWHM* at $z = 0.8$ (0.″6 *FWHM* in $I$) respectively. Even though the sampling of the ACS and FORS2 images differs by a factor of seven, their limits on $B/T$ and $S2$ for the computation of consistent early-type galaxy fractions were quite similar. This is an indication of the robustness of our measured structural parameters over this range of spatial resolutions. For the sake of simplicity, we therefore adopt the ACS limits ($(B/T)_{{\rm SDSS},g} \ge 0.35$ and $S2_{{\rm SDSS},g} \le 0.075$) for our SDSS early-type galaxy fractions rather than use yet another set of limits. We can further test these limits on the catalogue of visually classified galaxies from the SDSS North Equatorial Region of Fukugita et al. (2007). This catalogue contains Hubble T-type visual classifications for 2253 galaxies down to a magnitude limit of $r = 16$. If we apply our limits on $(B/T)_{{\rm SDSS},g}$ and $S2_{{\rm SDSS},g}$ to galaxies in this catalogue, then we find that the coefficients of the SDSS-to-visual equivalent of Eq. (4) would be 0.88, 0.68, 0.14, and 0.014 respectively. Early-type SDSS galaxies are therefore quantitatively selected with an "efficiency" comparable to our selection from the ACS images.

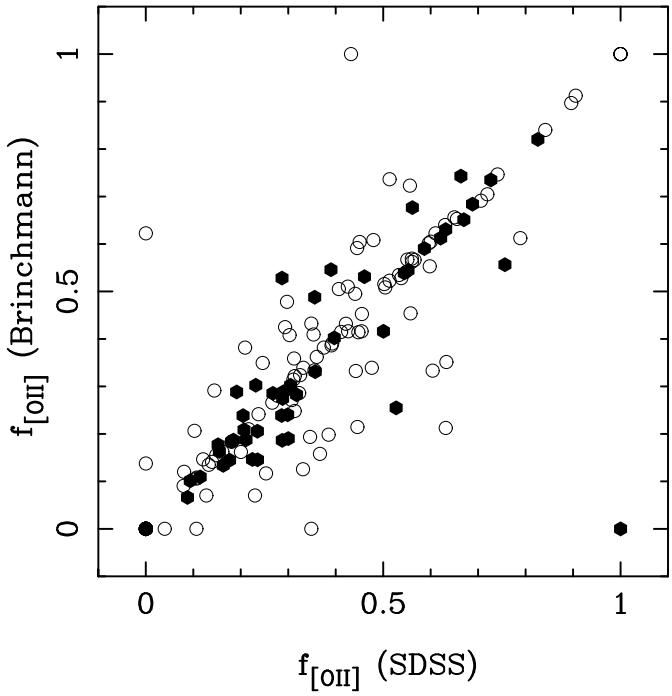


**Fig. 6.** Comparison between fractions of [OII] emitters computed using emission-line measurements from Brinchmann et al. (2004) and the DR7 release. Filled and open circles are clusters with $\sigma \ge 600$ km s$^{-1}$ and $\sigma < 600$ km s$^{-1}$ respectively.

The raw fractions of [OII] emitters for the 158 SDSS-C4 clusters were calculated by directly querying the SDSS database table SpecLine for the [OII]3727 and [OII]3730 equivalent widths for each confirmed cluster member, adding them together and correcting them to rest-frame by dividing by $(1 + z)$. The corrected [OII] fractions were then computed following exactly the same calculations (and using the same weights, the same luminosity and clustercentric radius cuts of $M_V \le -19.8$ and $R \le 0.6\,R_{200}$) as for the early-type fractions except that the early-type selection criteria on bulge fraction and image smoothness were simply replaced by the Poggianti et al. (2006) cut of $EW([{\rm OII}]) \le -3$ Å. In order to evaluate the importance of the errors on our equivalent widths on our determination of the fractions of [OII] emitters, we also computed [OII] fractions using equivalent widths from Brinchmann et al. (2004). The two sets of equivalent widths are plotted against one another in Fig. 6. The agreement between the two sets is excellent, and we conclude that our [OII] fractions are robust.

Table 4 gives corrected early-type galaxy fractions and fractions of [OII] computed for $R \le 0.6\,R_{200}$ for the 158 SDSS clusters in our local comparison sample. We included only galaxies brighter than $M_{V,{\rm lim}} = -19.8$ to avoid incompleteness in the SDSS spectroscopic sample. This cutoff magnitude corresponds to the absolute magnitude limits we used for our distant EDisCS clusters once passive evolution is taken into account (see Sect. 4.2).

### 4.5. Theoretical models

Numerical simulations of dark matter haloes populated with galaxies using semi-analytical models greatly help in the interpretation of observational results. We use here the Millennium Simulation (MS; Springel et al. 2005), and the semi-analytical

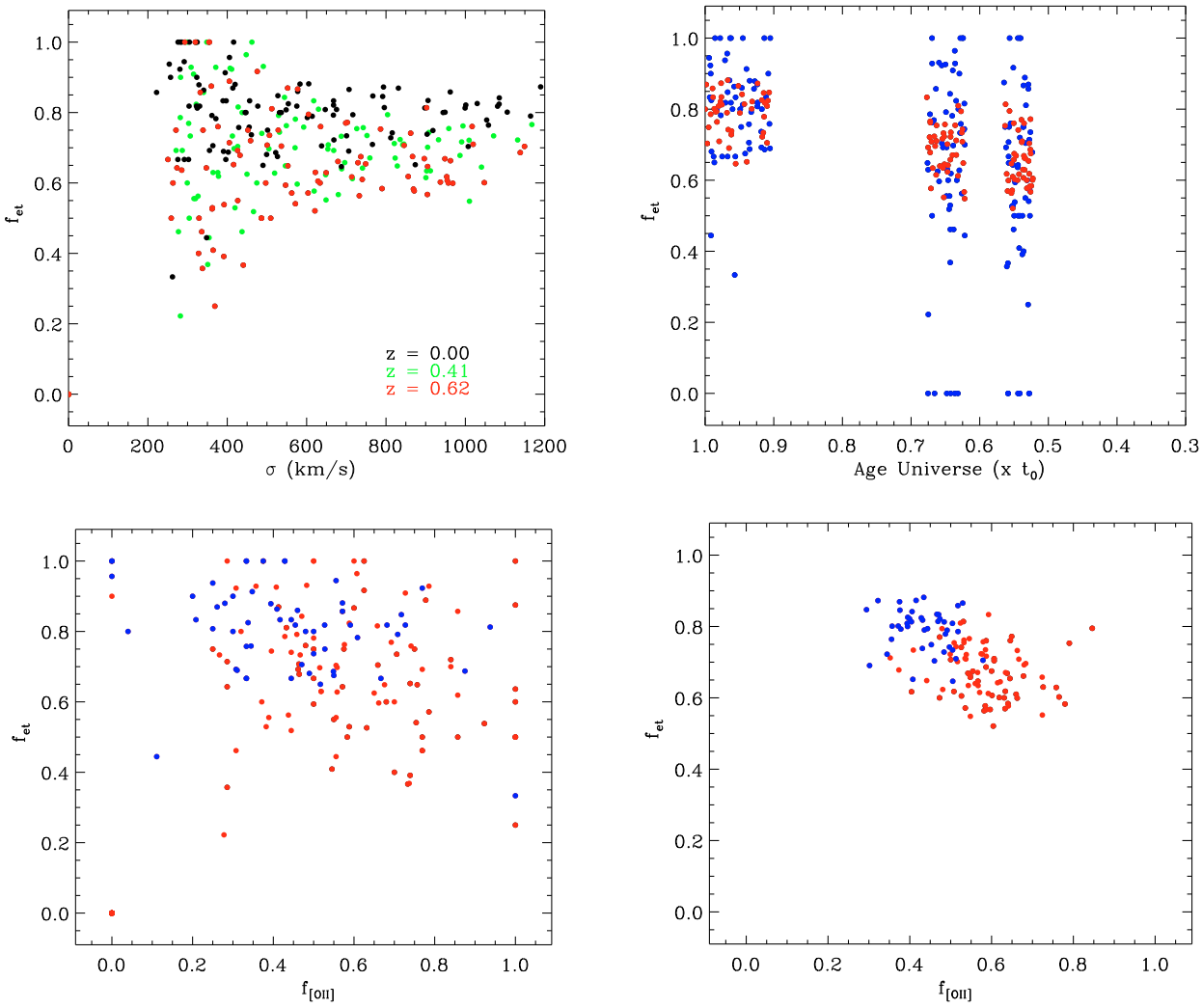


**Fig. 7.** Early-type galaxies in Millennium Simulation dark matter haloes *Top, left-hand panel*: early-type galaxy fraction within 0.6 $R_{200}$ versus cluster velocity dispersion at three different redshifts. *Top, right-hand panel*: early-type galaxy fraction within 0.6 $R_{200}$ versus age of the universe. Blue and red points are clusters with velocity dispersions below and above 600 km s$^{-1}$ respectively. *Lower, left-hand panel*: early-type galaxy fraction within 0.6 $R_{200}$ versus fraction of star-forming galaxies in clusters with $\sigma < 600$ km s$^{-1}$. Blue points show haloes selected at redshift zero, and all the other haloes are in red. *Lower, right-hand panel*: early-type galaxy fraction within 0.6 $R_{200}$ versus fraction of star-forming galaxies in clusters with $\sigma \geq 600$ km s$^{-1}$.

code described in De Lucia & Blaizot (2007)[2]. The MS followed $2160^3$ particles of mass $8.6 \times 10^8\ h^{-1}\ M_\odot$ within a comoving box of size 500 $h^{-1}$ Mpc on a side with a spatial resolution of 5 $h^{-1}$ kpc. Early-type galaxy fractions were computed from these simulated galaxy catalogs using the following procedure. Haloes were randomly selected at three different redshifts ($z$ = 0, 0.41, 0.62) so that they were uniformly distributed in $\log(M_{200})$. The final halo sample was 100 haloes at $z$ = 0, 94 haloes at $z$ = 0.41 and 92 haloes at $z$ = 0.62. For each of these haloes, all galaxies in a cubic box 6 Mpc on a side around the central galaxy were selected, and a morphological type was assigned to each model galaxy by computing the quantity $\Delta M = M_{\rm bulge} - M_{\rm total}$ (in the rest-frame $B$-band). Galaxies with $\Delta M < 1.0$ were considered to be "early-type". This is the same criterion as selecting real galaxies with $B/T_{\rm FORS2} \geq 0.40$. It is important here to note that an early-type galaxy in the simulations was defined solely based on this cut in bulge fraction because the simulations do not have the resolution required to model internal fine structures such as asymmetries. Given that real, early-type galaxies were also selected according to image smoothness, one might find the early-type fractions of real clusters to be systematically lower. For each halo, the fraction of early-type galaxies within 0.6 $R_{200}$ from the BCG was computed using three different projections. Furthermore, only galaxies that were within 2 Mpc from the BCG along the line of sight were included. The fractions were computed using only galaxies brighter than −20.5, −20.1, and −19.8 in the rest-frame $V$-band at redshift 0.6, 0.4, and 0.0 respectively to match the limits used for the SDSS and EDisCS early-type galaxy fractions. A galaxy in the simulation was deemed to be star-forming if its star-formation rate in the last timestep of its evolution was not equal to zero.

Figure 7 shows the resulting model early-type fractions as a function of cluster velocity dispersion, redshift and fraction of star-forming galaxies for the MS haloes. At a given redshift, there is no dependence of the early-type fraction on cluster velocity dispersion, but the scatter symmetrically increases towards both lower and higher fractions leading to a "wedge-like" distribution towards lower cluster $\sigma$'s. The early-type fractions

[2] Simulated galaxy catalogs used here are publicly available at http://www.mpa-garching.mpg.de/millennium/

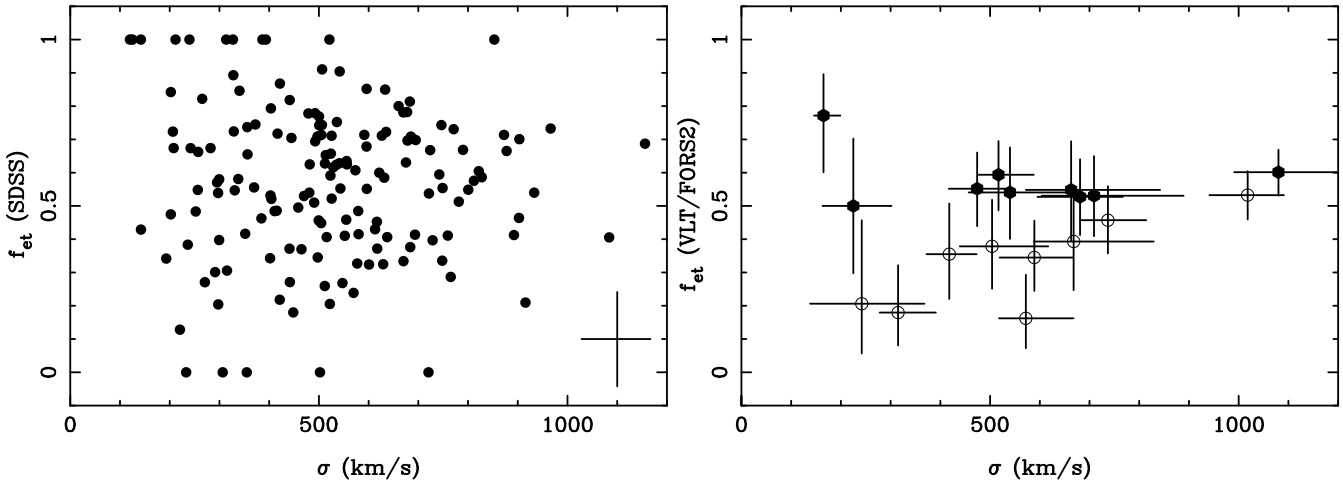


**Fig. 8.** Early-type galaxy fraction within 0.6 $R_{200}$ versus velocity dispersion for SDSS and EDisCS clusters. Both samples have been matched in velocity dispersion. *Left panel*: SDSS clusters. Only typical error bars are shown in the lower right-hand corner for clarity. *Right panel*: filled and open circles are mid-$z$ and high-$z$ EDisCS clusters respectively. Errors bars shown in both panels are 1$\sigma$ errors. Our VLT/FORS2 early-type fractions are used here for all EDisCS clusters for the sake of uniformity.

of both low and high-mass clusters increase with decreasing redshift from ~0.70 at $z = 0.65$ to ~0.85 at $z = 0$. The early-type fractions of massive clusters are anticorrelated with the fractions of star-forming galaxies: clusters at $z = 0$ have higher early-type fractions but lower fractions of star-forming galaxies. Note that the trends in Fig. 7 do not agree with those shown in Diaferio et al. (2001) although the assumptions made about morphological transformations are very similar in the two models. In particular, the MS shows little trend of early-type fraction with cluster velocity dispersion but a substantial trend with redshift, while Diaferio et al. found the opposite. This is likely a result of the poorer mass resolution, poorer statistics and cruder dynamical modelling of the earlier paper.

## 5. Results

We use here our VLT/FORS2 early-type fractions for all EDisCS clusters for the sake of uniformity.

### 5.1. Early-type galaxy fractions versus cluster velocity dispersion and redshift

Figure 8 shows early-type galaxy fractions versus velocity dispersion for the SDSS and EDisCS clusters. The early-type galaxy fractions of both cluster samples exhibit no clear trend as a function of $\sigma$. Table 5 gives Spearman rank test results for the SDSS sample and different EDisCS subsamples. The only significant correlation between early-type fraction and velocity dispersion is found in the high-$z$ EDisCS clusters. It only has a 2.5% chance of being due to randon sampling. Such a positive correlation was also reported in Desai et al. (2007) for the same cluster subsample, but it disappears when the full EDisCS sample is considered. The lack of a significant correlation agrees well with the results for the Millennium Simulation in the top left-hand panel of Fig. 7 but disagrees with the earlier theoretical results of Diaferio et al. (2001) which showed a trend between $f_{et}$ and $\sigma$. A visual inspection of Fig. 8 confirms the statistical test results. The mid-$z$ EDisCS clusters do not show any correlation with $\sigma$ in contrast to the high-$z$ clusters. In particular, two mid-$z$ EDisCS clusters (CL1119.3-1130 and CL1420.3-1236) with $\sigma \sim 200$ km s$^{-1}$ have early-type fractions similar or higher ($f_{et} \sim 0.5$–$0.8$) than the most massive clusters in our sample. Interestingly, the same two clusters were found by Poggianti et al. (2006) to be the most outstanding outliers in the [OII] fraction – $\sigma$ relation in the sense that they have a low fraction of [OII] emitters for their mass. This is consistent with what we observe here given that early-type galaxies typically have lower [OII] emission fluxes.

**Table 5.** Spearman rank test results for early-type fraction versus cluster velocity dispersion.

| Cluster sample | $N_{cl}$ | $R_s$ | $p$-value |
|---|---|---|---|
| (1) | (2) | (3) | (4) |
| SDSS | 158 | −0.05 | 0.51 |
| EDisCS all | 18 | 0.18 | 0.47 |
| EDisCS mid-$z$ | 9 | −0.11 | 0.78 |
| EDisCS high-$z$ | 9 | 0.73 | 0.025 |

Figure 8 does show that there is a marked difference in the morphological content of the EDisCS and SDSS clusters. All EDisCS $f_{et}$ values (with the exception of one cluster) are below 0.6, but half of the SDSS clusters are above this value. The population of early-type galaxies has thus increased significantly in half of the clusters *of all velocity dispersions*. An increase in early-type fraction with decreasing redshift may already be visible when one compares mid-$z$ and high-$z$ EDisCS clusters. Mid-$z$ clusters around $\sigma = 500$ km s$^{-1}$ have $f_{et} \simeq 0.5$ whereas the high-$z$ clusters have $f_{et} \simeq 0.4$. This would represent a ~25% increase over a time interval of 2 Gyr. As shown in Fig. 7, the early-type fractions of clusters in the Millenium Simulation also increase with decreasing redshift in clusters of all velocity dispersions, but there is a lack of simulated clusters with $f_{et} < 0.5$ compared with the SDSS-C4 clusters. The scatter in the $f_{et}$ values of simulated clusters is also smaller than in those of real clusters. For simulated clusters at $z = 0$ with $\sigma \geq 600$ km s$^{-1}$, $\sigma(f_{et}) = 0.06$ compared to $\sigma(f_{et}) = 0.21$ for SDSS clusters over the same range of velocity dispersions. Given that the mean error on the SDSS $f_{et}$ values is 0.12, the intrinsic scatter would be 0.17. This intrinsic scatter is still almost three times the scatter in the simulated clusters.

Figure 9 shows SDSS and EDisCS early-type fractions as a function of the age of the universe (i.e., redshift). The clusters have been divided into two subgroups based on their

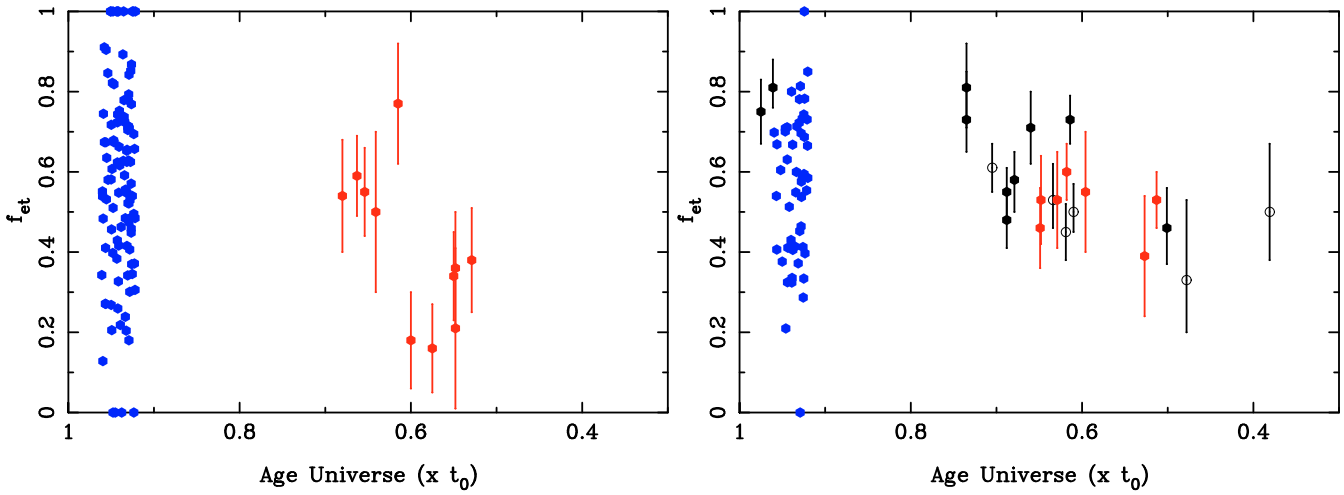


**Fig. 9.** Early-type galaxy fraction versus age of the universe (i.e., redshift) for clusters with $\sigma < 600$ km s$^{-1}$ (left panel) and clusters with $\sigma \geq 600$ km s$^{-1}$ (right panels). SDSS and EDisCS clusters are blue and red respectively, and both samples have been matched in velocity dispersion. Clusters shown in black are from the compilation of van Dokkum et al. (2001) in which open and solid points have X-ray luminosities below and over $10^{44.5}$ erg s$^{-1}$ respectively. Our VLT/FORS2 early-type fractions are used here for all EDisCS clusters for the sake of uniformity.

velocity dispersions. The early-type fractions of massive ($\sigma >$ 600 km s$^{-1}$) EDisCS clusters (right panel) are in very good agreement with the ones in the compilation of van Dokkum et al. (2001) which also have velocity dispersions greater than 600 km s$^{-1}$. The clusters at low redshift in the van Dokkum et al. (2001) compilation suggest that there are no local clusters with low early-type fractions and hence that all clusters have uniformly increased their early-type fraction from $z \sim 0$. to the present day. However, our SDSS cluster sample shows that this simple picture is not entirely true. While half of the SDSS clusters have higher early-type fractions than clusters at high redshift, the other half have early-type fractions equal or even lower than the EDisCS clusters. The same holds true for the low mass clusters (left-hand panel). The scatter in $f_{et}$ (<0.1) in high-mass EDisCS clusters does appear to be considerably less that the scatter seen in low-mass clusters.

The lack of a clear trend in early-type fraction with redshift in the right-hand panel of Fig. 9 is in disagreement with the Millennium Simulation prediction in the top right-hand panel of Fig. 7. There is a clear deficit of clusters with low early-type fraction at low redshift in the Millenium Simulation compared with our SDSS sample.

### 5.2. Early-type galaxy fractions versus fractions of [OII] emitters

The link between star formation and morphological transformation and its evolution as a function of redshift provides more clues on the processes driving galaxy morphology in local and distant clusters. The fractions of galaxies with [OII] emission in the EDisCS clusters were computed as in Poggianti et al. (2006) using the same absolute magnitude limits and the same prescriptions for correcting magnitude and geometric incompletness, but the clustercentric radius cut was changed to match the one used for the early-type fractions in this paper ($R_{et} \leq 0.6\ R_{200}$). The two datasets are therefore directly comparable. Figure 10 shows $f_{et}$ versus $f_{[OII]}$ with our local and distant samples again divided according to velocity dispersion. Table 7 gives Spearman test results between $f_{et}$ and $f_{[OII]}$. There is a strong correlation between $f_{et}$ versus $f_{[OII]}$ in both SDSS and EDisCS cluster samples irrespective of cluster velocity dispersion. The EDisCS clusters lie within the envelopes defined by the SDSS clusters. There is no offset between the zeropoints of the correlations at low and high redshift. However, as demonstrated by Poggianti et al. (2006), the star formation activity (parametrized by $f_{[OII]}$) has decreased in all environments from $z \sim 0.75$ to $z \sim 0.08$. This is confirmed by the K-S test results in Table 8. The probabilities that the EDisCS and SDSS clusters are drawn from the same parent $f_{[OII]}$ distribution are only 0.026, 0.005 and 0.046 for the whole samples, low $\sigma$ and high $\sigma$ subsamples respectively.

The $f_{et}$ versus $f_{[OII]}$ values for clusters from the Millenium Simulation (Fig. 7) are quite different from the observations. Low $\sigma$ MS clusters at low and high redshifts are confined to high $f_{et}$ and $f_{OII}$ values with no apparent correlation. There is only a handful of clusters with low values for both $f_{et}$ and $f_{OII}$. The high $\sigma$ MS clusters are found in a very limited range of $f_{et}$ and $f_{OII}$ values ($0.35 < f_{OII} < 0.75$, $0.6 < f_{et} < 0.85$).

## 6. Discussion

In order to fully understand possible evolutionary trends observed here, it is important to determine how cluster velocity dispersion changes with redshift as a result of the hierarchical growth of structures. Are we looking at similar clusters when we focus on the same range of velocity dispersions in the SDSS and EDisCS clusters? Poggianti et al. (2006) looked at the mean change in $\sigma$ between $z = 0$ and $z = 0.76$ using a sample of 90 haloes from the Millennium Simulation uniformly distributed in log(mass) between $5 \times 10^{12}$ and $5 \times 10^{15}$ $M_{\odot}$. Their Fig. 8 shows how $\sigma$ evolves over that redshift interval. For example, a $z = 0$ cluster with $\sigma = 900$ km s$^{-1}$ would typically have $\sigma \sim$ 750 km s$^{-1}$ at $z = 0.76$. This evolution is not sufficient to introduce biases in our analysis here. Indeed, selecting clusters with $\sigma \geq 600$ km s$^{-1}$, say, at either $z = 0$ or $z = 0.76$ would keep nearly all the same clusters. Measured velocity dispersions may exhibit a large scatter with respect to the true halo mass particularly for low-mass clusters. The velocity dispersions for the SDSS and EDisCS clusters were calculated in a very similar way in order to minimize any biases. Velocity dispersions calculated from a small number of cluster members may be overestimates of the true cluster mass. Table 1 lists 1103.7-1245b as the cluster with the lowest number of members ($N = 11$). In order to check the

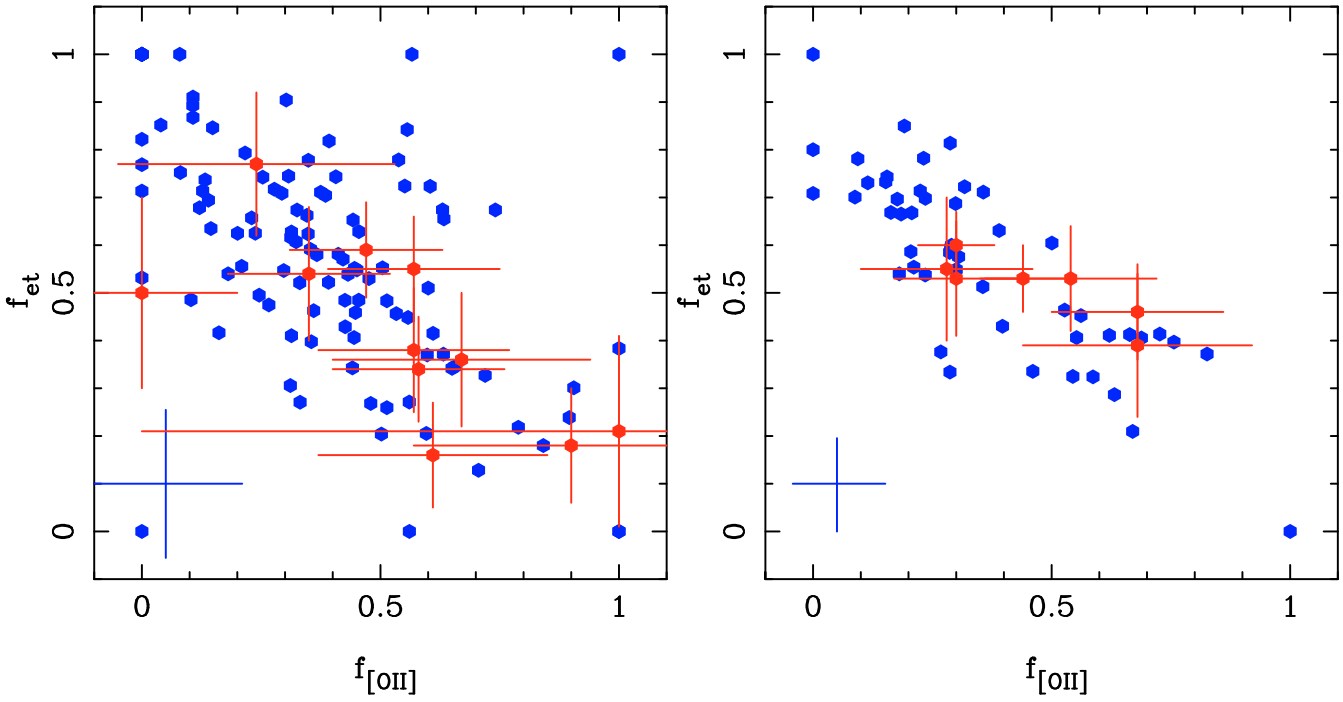


**Fig. 10.** Early-type galaxy fraction versus [OII] emitter fraction for clusters with $\sigma < 600$ km s$^{-1}$ (*left panel*) and clusters with $\sigma \geq 600$ km s$^{-1}$ (*right panel*). SDSS and EDisCS clusters are shown in blue and red respectively, and both samples have been matched in velocity dispersion. Only typical error bars are shown for the SDSS clusters in the lower right-hand corner for clarity. Our VLT/FORS2 early-type fractions are used here for all EDisCS clusters for the sake of uniformity.

**Table 6.** Two-sample Kolmogorov-Smirnov test probabilities for early-type fraction versus cluster velocity dispersion.

| | Cluster sample 2 | | | |
|---|---|---|---|---|
| Cluster sample 1 | SDSS (All) | SDSS ($\sigma \geq 600$) | EDisCS ($\sigma < 600$) | EDisCS ($\sigma \geq 600$) |
| SDSS ($\sigma < 600$) | ... | 0.628 | 0.190 | ... |
| SDSS ($\sigma \geq 600$) | ... | ... | ... | 0.472 |
| EDisCS ($\sigma < 600$) | ... | ... | ... | 0.250 |
| EDisCS (All) | 0.506 | ... | ... | ... |

**Table 8.** Two-sample Kolmogorov-Smirnov test probabilities for [OII] emitter fraction versus cluster velocity dispersion.

| | Cluster sample 2 | | | |
|---|---|---|---|---|
| Cluster Sample 1 | SDSS (All) | SDSS ($\sigma \geq 600$) | EDisCS ($\sigma < 600$) | EDisCS ($\sigma \geq 600$) |
| SDSS ($\sigma < 600$) | ... | 0.090 | 0.005 | ... |
| SDSS ($\sigma \geq 600$) | ... | ... | ... | 0.046 |
| EDisCS ($\sigma < 600$) | ... | ... | ... | 0.761 |
| EDisCS (All) | 0.026 | ... | ... | ... |

**Table 7.** Spearman rank test results for early-type fraction versus fraction of [OII] emitters.

| Cluster sample (1) | $N_{cl}$ (2) | $R_s$ (3) | $p$-value (4) |
|---|---|---|---|
| SDSS (All) | 158 | −0.63 | $4.33 \times 10^{-19}$ |
| SDSS ($\sigma < 600$) | 108 | −0.57 | $1.50 \times 10^{-10}$ |
| SDSS ($\sigma \geq 600$) | 50 | −0.77 | $6.04 \times 10^{-11}$ |
| EDisCS (All) | 18 | −0.74 | 0.00043 |
| EDisCS ($\sigma < 600$) | 11 | −0.78 | 0.0043 |
| EDisCS ($\sigma \geq 600$) | 7 | −0.77 | 0.0438 |

robustness of our results, we re-ran our analyses by excluding SDSS clusters in Table 4 with $N < 10$ for which velocity dispersions may be less reliable and found that our results remained unchanged.

Poggianti et al. (2006) proposed a scenario in which two channels are responsible for the production of passive galaxies in clusters, and others (Faber et al. 2007; Brown et al. 2007) have proposed a similar scenario for the migration of galaxies from the "blue cloud" to the red sequence. "Primordial passive galaxies" are composed of galaxies whose stars all formed at very high redshift ($z > 2$) over a short timescale. These galaxies have been observed in clusters up and beyond $z = 1$, and they largely comprise luminous ellipticals. "Quenched passive galaxies" have had a more extended period of star formation activity, and their star formation has been quenched after their infall into dense cluster environments. These quenched passive galaxies would then suffer the effects of cluster processes such as ram pressure stripping, harassment, strangulation and mergers to become S0 and earlier type galaxies. A key point of this scenario is that processes affecting morphology and star formation activity operate on different timescales as shown recently for the EDisCS sample by Sánchez-Blázquez et al. (2009). There is good evidence that star formation is quenched in galaxies over timescales of 1−3 Gyr after they have entered the cluster environment (Poggianti et al. 1999, 2006) whereas morphological transformation through mergers and harassment can take longer (~5 Gyr, Moore et al. 1998). The best example of this is the fact that the vast majority of post-starburst galaxies in distant clusters, those that have had their star formation activity terminated during the last Gyr, still retain a spiral morphology (Poggianti et al. 1999). Such a two-channel scenario would naturally explain observations indicating that the elliptical galaxy fraction

actually remains constant with redshift while the S0 fraction rises with decreasing redshift (Dressler et al. 1997; Fasano et al. 2000; Desai et al. 2007). Unfortunately, the VLT/FORS2 images do not have sufficient spatial resolution to disentangle E and S0 galaxies as mentioned in Sect. 4.1 to determine the exact contribution from each channel. We can therefore only study the overall production of early-type galaxies, but it should exhibit different behaviors with cluster global properties depending on the process(es) dominating it. Given our quantitative definition of an early-type galaxy based on bulge fraction and image smoothness, there are essentially two ways to transform late-type galaxies into early-type ones: 1) processes such as collisions and harassment that can fundamentally alter the structure of a galaxy by forming bulges and/or destroying disks and 2) quenching processes that can extinguish star forming regions responsible for some of the galaxy image asymmetries and also cause a fading of the disks.

Applying the Poggianti et al. (2006) scenario to our results, the "threshold" in $f_{\rm et}$ values in our high redshift clusters (Figs. 8 and 9) could be explained by a population of primordial passive galaxies that formed at even higher redshifts. Most of our high redshift clusters have early-type fractions in the range 0.3−0.6 with no correlation with cluster velocity dispersion. Are these early-type fractions indeed consistent with a populations of primordial passive galaxies? Calculations done in Poggianti et al. (2006) show that the fraction of galaxies at $z = 0.6$ that were present in haloes with masses greater than $3 \times 10^{12}\ M_{\odot}$ at $z = 2.5$ is $0.4 \pm 0.2$. These primordial passive galaxies can therefore account for at least 2/3 (if not all) of the early-type populations in high redshift clusters, and their high formation redshift would explain the lack of dependence of $f_{\rm et}$ on cluster velocity dispersion.

One of our main results is that the early-type fractions of galaxy clusters increase from $z = 0.6$−$0.8$ to $z \sim 0.08$ in clusters of all velocity dispersions. What kind of morphological transformation process(es) can lead to such an evolution? Collisions and harassment both depend on galaxy-galaxy interactions and the time a galaxy has spent within the cluster environment. Cluster velocity dispersion influences the number of interactions and their duration. Higher velocity dispersions in more massive clusters yield more interactions per unit time $N$ but with shorter durations $\Delta t$ in a given time interval. One might therefore expect to see a peak in early-type type fraction at the cluster velocity dispersion where the product $N\Delta t$ is maximized. No such peak is seen in our clusters. Ram-pressure stripping is expected to go as $(n_{\rm ICM} v_{\rm gal}^{2.4})/\dot{M}_{\rm rep}$ (Gaetz et al. 1987) with $n_{\rm ICM}$, $v_{\rm gal}$ and $\dot{M}_{\rm rep}$ being the density of the ICM, the velocity of the galaxies within the ICM and the rate at which galaxies can replenish their gas respectively. The fraction of passive galaxies should therefore be a relatively strong function of cluster velocity dispersion if quenching by ram pressure stripping is the dominant process. The number of post-starburst galaxies in EDisCS clusters does correlate with cluster velocity dispersion (Poggianti et al. 2009a), but the uniform increase in early-type fractions at all cluster velocity dispersions observed going from EDisCS to SDSS clusters is not consistent with the intracluster medium being the main cause of the changes in cluster morphological content.

Even though the EDisCS and SDSS early-type fractions show no correlation with cluster velocity dispersion, and the SDSS [OII] emitter fractions (but not the EDisCS ones) also show no such correlation (Poggianti et al. 2006; Popesso et al. 2007), there is a very strong correlation between $f_{\rm et}$ and $f_{\rm OII}$. This correlation is seen at both low and high cluster masses as well as at both low and high redshifts. Morphology and star formation therefore appear to be closely linked with one another over a wide range of environments and times. However, different structural transformation and quenching processes are thought to operate over different timescales (e.g., Sánchez-Blázquez et al. 2009). Timescales range from 1−2 Gyr (based on typical cluster crossing times) for truncating star formation to 3−5 Gyr for totally extinguishing star formation in newly accreted galaxies (Poggianti et al. 2006; Tonnesen & Bryan 2009). Looking at the evolution of EDisCS cluster red-sequence galaxies over 2 Gyr (from $z = 0.75$ to $z = 0.45$), Sánchez-Blázquez et al. (2009) found that morphological transformation and quenching of star formation indeed appeared to not be simultaneous. As noted in Sect. 5.1, the early-type fractions of mid-$z$ EDisCS clusters may be ∼25% higher than the ones of high-$z$ clusters. This change would therefore have taken place over a 2 Gyr interval in our adopted cosmology. However, the time baseline here between SDSS and EDisCS clusters is almost 6 Gyr, and, unfortunately, this is ample time to erase any difference arising from different timescales in the link between morphology and star formation.

The lack of dependence of morphology and star formation on global cluster properties such as velocity dispersion raises the question of whether changes in galaxy properties are driven by more local effects or whether they occur outside of the cluster environment. Recent work (Poggianti et al. 2008; Park & Choi 2009; Bamford et al. 2009; Ellison et al. 2009) have re-emphasized the strong link between galaxy properties and local galaxy density rather than cluster membership. Galaxy properties are seen to change at densities around 15−40 galaxies Mpc$^{-2}$ or projected separations of $20$−$30\ h^{-1}$ kpc. Others (e.g., Kautsch et al. 2008; Wilman et al. 2009) have suggested that the galaxy group environment might be more conducive to galaxy transformation. Our observed evolution in early-type fraction as a function of redshift and the strong correlation between morphology and star formation at all cluster masses would support the idea that cluster membership is of lesser importance than other variables such as local density in determining galaxy properties.

The properties of simulated clusters from the Millenium Simulation compare well with those of EDisCS and SDSS clusters. Their early-type fractions also show no dependence with cluster velocity dispersion in contrast to previous theoretical work (e.g. Diaferio et al. 2001) but in agreement with observations. However, there is a definite lack of MS clusters with low early-type fractions at $z = 0$ compared to the SDSS sample. It is important here to note that an early-type galaxy in the simulations was defined solely based on its bulge fraction because the simulations do not have the resolution required to model internal fine structures such as asymmetries. Given that real, early-type galaxies were also selected according to image smoothness, one would expect the early-type fractions of real clusters to be systematically lower. However, half of the SDSS clusters have low early-type fractions not seen in the simulations at $z = 0$, and such a large discrepancy could only be explained by a significant population of real bulge-dominated galaxies with relatively large asymmetries. It is more likely that bulge formation in the simulations may be too efficient. The scatter in $f_{\rm et}$ values for the simulated clusters with $\sigma \geq 600$ km s$^{-1}$ is also nearly three times smaller than observed in the real clusters (Sect. 5.1) which may indicate that the models may not include the right mixture of evolutionary processes at work on real galaxies. High-mass simulated clusters show a correlation between early-type fraction and star-forming fraction (albeit over narrower ranges than observed), but the correlation is not seen in the low-mass

simulated clusters. This may be understood by high mass clusters having been formed long enough for evolutionary processes to have had enough time to act on galaxies to modify their properties whereas this is not necessarily the case for low-mass clusters. The fact that the correlation is observed in both low- and high-mass real clusters may be an indication that processes giving rise to the correlation may be more efficient (or altogether different) than modelled. It is also important to keep in mind here that the properties of a galaxy in these models are essentially driven by the mass of its parent halo.

## 7. Summary

We have presented quantitative morphologies measured from PSF-convolved, 2D bulge+disk decompositions of cluster and field galaxies on deep VLT/FORS2 images of eighteen, optically-selected galaxy clusters at $0.45 < z < 0.80$ observed as part of the ESO Distant Cluster Survey. The morphological content of these clusters was characterized by the early-type fraction within a clustercentric radius of $0.6\,R_{200}$, and early-type galaxies were selected based on bulge fraction and image smoothness. We showed a very good agreement between quantitative and visual galaxy classifications. We used a set of 158 clusters extracted from the Sloan Digital Sky Survey matched in velocity dispersion to our EDisCS sample and analyzed exactly in the same way to provide a robust comparison baseline and to control systematics. We studied trends in early-type fraction as a function of cluster mass and redshift. We also explored the link between morphology and star formation by comparing early-type fractions to the fractions of [OII] emitters in our clusters. Our main results are:

1. The early-type fractions of the SDSS and EDisCS clusters exhibit no clear trend as a function of cluster velocity dispersion.
2. Mid-$z$ EDisCS clusters around $\sigma = 500\,\mathrm{km\,s^{-1}}$ have $f_{\mathrm{et}} \simeq 0.5$ whereas high-$z$ EDisCS clusters have $f_{\mathrm{et}} \simeq 0.4$. This represents a ~25% increase over a time interval of 2 Gyr.
3. There is a marked difference in the morphological content of the EDisCS and SDSS samples. None of the EDisCS clusters have an early-type fraction greater than 0.6 whereas half of the SDSS clusters lie above this value. *This difference is seen in clusters of all velocity dispersions (i.e., masses).*
4. There is a strong and clear correlation between morphology and star formation activity in the sense that decreasing fractions of [OII] emitters are tracked by increasing early-type fractions. This correlation holds in both low and high cluster masses as well as at both low and high redshift.
5. The early-type fractions of clusters drawn from the Millennium Simulation (Springel et al. 2005) using the galaxy formation model of De Lucia & Blaizot (2007) also show no clear dependence on cluster velocity dispersion. However, at $z = 0$, they are not enough simulated clusters with low early-type fractions compared to the SDSS cluster sample. While high-mass simulated clusters show a correlation between early-type fraction and star-forming fraction (albeit over narrower ranges than observed), this correlation is not seen in the low-mass simulated clusters in contrast to the real ones.

Our results pose an interesting challenge to structural transformation and star formation quenching processes that strongly depend on the global cluster environment (e.g., a dense ICM) and suggest that cluster membership may be of lesser importance than other variables in determining galaxy properties.

*Acknowledgements.* We are thankful to the anonymous referee for suggestions that greatly contributed this paper. We have benefitted from the generosity of the ESO/OPC. G.R. thanks Special Research Area No 375 of the German Research Foundation for financial support. The Millennium Simulation databases used in this paper and the web applications providing access to them were constructed as part of the activities of the German Astrophysical Virtual Observatory. Funding for the creation and distribution of the SDSS Archive has been provided by the Alfred P. Sloan Foundation, the Participating Institutions, the National Aeronautics and Space Administration, the National Science Foundation, the US Department of Energy, the Japanese Monbukagakusho, and the Max Planck Society. The SDSS Web site is http://www.sdss.org/. The SDSS is managed by the Astrophysical Research Consortium (ARC) for the Participating Institutions. The Participating Institutions are The University of Chicago, Fermilab, the Institute for Advanced Study, the Japan Participation Group, The Johns Hopkins University, the Korean Scientist Group, Los Alamos National Laboratory, the Max-Planck-Institute for Astronomy (MPIA), the Max-Planck-Institute for Astrophysics (MPA), New Mexico State University, University of Pittsburgh, University of Portsmouth, Princeton University, the United States Naval Observatory, and the University of Washington. The Dark Cosmology Centre is funded by the Danish National Research Foundation.

## References

Abazajian, K., Adelman-McCarthy, J. K., Agüeros, M. A., et al. 2009, ApJS, 182, 543
Allen, S. W. 1998, MNRAS, 296, 392
Andredakis, Y. C. 1998, MNRAS, 295, 725
Balcells, M., Graham, A. W., Domínguez-Palmero, L., & Peletier, R. E. 2003, ApJ, 582, 79
Bamford, S. P., Nichol, R. C., Baldry, I. K., et al. 2009, MNRAS, 393, 1324
Barnes, J. E., & Hernquist, L. 1992, ARA&A, 30, 705
Barnes, J. E., & Hernquist, L. 1996, ApJ, 471, 115
Barazza, F. D., Jablonka, P., Desai, V., et al. 2009, A&A, 497, 713
Bessell, M. S. 1990, PASP, 102, 1181
Bertin, E., & Arnouts, S. 1996, A&AS, 117, 393
Blakeslee, J. P., Holden, B. P., Franx, M., et al. 2006, ApJ, 644, 30
Borgani, S., Girardi, M., Carlberg, R. G., Yee, H. K. C., & Ellingson, E. 1999, ApJ, 527, 561
Brinchmann, J., Charlot, S., White, S. D. M., et al. 2004, MNRAS, 351, 1151
Brown, M. J. I., Dey, A., Jannuzi, B. T., et al. 2007, ApJ, 654, 858
Carlberg, R. G., Yee, H. K. C., & Ellingson, E. 1997, ApJ, 478, 462
Clowe, D., Schneider, P., Aragón-Salamanca, A., et al. 2006, A&A, 451, 395
Courteau, S., de Jong, R. S., & Broeils, A. H. 1996, ApJ, 457, 73
de Jong, R. S. 1996, A&A, 118, 557
De Lucia, G., & Blaizot, J. 2007, MNRAS, 375, 2
De Lucia, G., Poggianti, B. M., Aragón-Salamanca, A., et al. 2004, ApJ, 610, 77
De Lucia, G., Poggianti, B. M., Aragón-Salamanca, A., et al. 2007, MNRAS, 374, 809
Desai, V., Dalcanton, J. J., Aragón-Salamanca, A., et al. 2007, ApJ, 660, 1151
Diaferio, A., Kauffmann, G., Balogh, M. L., et al. 2001, MNRAS, 323, 999
Dressler, A. 1984, ApJ, 281, 512
Dressler, A., Oemler, A., Jr., Couch, W. J., et al. 1997, ApJ, 490, 577
Ellison, S. L., Simard, L., Cowan, N. B., et al. 2009, MNRAS, 396, 1257
Faber, S. M., Willmer, C. N. A., Wolf, C., et al. 2007, ApJ, 665, 265
Farouki, R. T., & Shapiro, S. L. 1981, ApJ, 243, 32
Farouki, R. T., & Shapiro, S. L. 1982, ApJ, 259, 103
Fasano, G., Poggianti, B., Couch, W. J., et al. 2000, ApJ, 542, 673
Finn, R. A., Zaritsky, D., McCarthy, D. W. Jr., et al. 2005, ApJ, 630, 206
Fukugita, M., Nakamura, O., Okamura, S., et al. 2007, AJ, 134, 579
Gaetz, T. J., Salpeter, E. E., & Shaviv, G. 1987, ApJ, 316, 530
Gladders, M. D., & Yee, H. K. C. 2005, ApJS, 157, 1
Gonzalez, A. H., Zaritsky, D., Dalcanton, J. J., & Nelson, A. 2001, ApJS, 137, 117
Gonzalez, A. H., Zaritsky, D., Simard, L., Clowe, D., & White, S. D. M. 2002, ApJ, 579, 577
Gunn, J. E., & Gott, J. R. I. 1972, ApJ, 176, 1
Halliday, C., Milvang-Jensen, B., Poirier, S., et al. 2004, A&A, 427, 397
Hoekstra, H., Franx, M., & Kuijken, K. 2000, ApJ, 532, 88
Holden, B. P., Stanford, S. A., Eisenhardt, P., & Dickinson, M. 2004, ApJ, 127, 2484
Holden, B. P., Illingworth, G. D., Franx, M., et al. 2007, ApJ, 670, 190
Holden, B. P., Franx, M., Illingworth, G. D., et al. 2009, ApJ, 693, 617
Im, M., Simard, L., Faber, S. M., et al. 2002, ApJ, 571, 136
Johnson, O., Best, P., Zaritsky, D., et al. 2006, MNRAS, 371, 1777
Kaiser, N., & Squires, G. 1993, ApJ, 404, 441
Kautsch, S. J., Gonzalez, A. H., Soto, C. A., et al. 2008, ApJ, 688, 5
Kormendy, J. 1985, ApJ, 295, 73

Lane, K. P., Gray, M. E., Aragón-Salamanca, A., Wolf, C., & Meisenheimer, K. 2007, MNRAS, 378, 716
Lanzoni, B., Guiderdoni, B., Mamon, G. A., Devriendt, J., & Hatton, S. 2005, MNRAS, 361, 369
Larson, R. B., Tinsley, B. M., & Caldwell, C. N. 1980, ApJ, 237, 692
Lin, D. N. C., & Faber, S. M. 1983, ApJ, 266, 17
Lubin, L. M., Oke, J. B., & Postman, M. 2002, AJ, 124, 1905
Martig, M., Bournaud, F., Teyssier, R., & Dekel, A. 2009, ApJ, submitted
McIntosh, D. H., Rix, H.-W., & Caldwell, N. 2002, ApJ, 610, 161
Milvang-Jensen, B., Noll, S., Halliday, C., et al. 2008, A&A, 482, 419
Mihos, J., & Hernquist, L. 1996, ApJ, 464, 641
Miller, C. J., Nichol, R. C., Reichart, D., et al. 2005, AJ, 130, 968
Moran, S. M., Ellis, R. S., Treu, T., et al. 2007, ApJ, 671, 1503
Moore, B., Katz, N., Lake, G., Dressler, A., & Oemler, A. 1996, Nature, 379, 613
Moore, B., Lake, G., & Katz, N. 1998, ApJ, 495, 139
Negroponte, J., & White, S. D. M. 1983, MNRAS, 205, 1009
Park, C., & Choi, Y.-Y. 2009, ApJ, 691, 1828
Pelló, R., et al. 2009, A&A, in press
Poggianti, B. M., Smail, I., Dressler, A., et al. 1999, ApJ, 518, 576
Poggianti, B. M., von der Linden, A., De Lucia, G., et al. 2006, ApJ, 642, 188
Poggianti, B. M., Desai, V., Finn, R., et al. 2008, ApJ, 684, 888
Poggianti, B. M., Aragón-Salamanca, A., Zaritsky, D., et al. 2009a, ApJ, 693, 112
Poggianti, B. M., Fasano, G., Bettoni, D., et al. 2009b, ApJ, 697, L137
Popesso, P., Biviano, A., Romaniello, M., & Böhringer, H. 2007, A&A, 461, 411
Postman, M., Franx, M., Cross, N. J. G., et al. 2005, ApJ, 623, 721
Quilis, V., Moore, B., & Bower, R. 2000, Science, 288, 1617
Rood, H. J., Page, T. L., Kintner, E. C., & King, I. R. 1972, ApJ, 175, 627
Rudnick, G., von der Linden, A., Pelló, R., et al. 2009, ApJ, 700, 1559
Sánchez-Blázquez, P., Jablonka, P., Noll, S., et al. 2009, A&A, 499, 47
Schneider, P., & Seitz, C. 1995, A&A, 294, 411
Simard, L., Willmer, C. N. A., Vogt, N. P., et al. 2002, ApJS, 142, 1
Smith, G. P., Treu, T., Ellis, R. S., Moran, S. M., & Dressler, A. 2005, ApJ, 620, 78
Spitzer, L. J., & Baade, W. 1951, ApJ, 113, 413
Springel, V., White, S. D. M., Jenkins, A., et al. 2005, Nature, 435, 629
Steinmetz, M., & Navarro, J. F. 2002, New Astron., 7, 155
Stetson, P. B. 1987, PASP, 99, 191
Tonnesen, S., & Bryan, G. L. 2009, ApJ, 694, 789
Toomre, A., & Toomre, J. 1972, ApJ, 178, 623
Tran, K.-V. H., Kelson, D. D., van Dokkum, P., et al. 1999, ApJ, 522, 39
Tran, K.-V. H., Simard, L., Illingworth, G. D., & Franx, M. 2003, ApJ, 590, 238
van der Wel, A., Holden, B. P., Franx, M., et al. 2007, ApJ, 670, 206
van Dokkum, P. G., Franx, M., Fabricant, D., Illingworth, G. D., & Kelson, D. D. 2000, ApJ, 541, 95
van Dokkum, P. G., Stanford, S. A., Holden, B. P., et al. 2001, ApJ, 552, 101
von der Linden, A., Best, P. N., Kauffmann, G., & White, S. D. M. 2007, MNRAS, 379, 867
White, S. D. M., Clowe, D. I., Simard, L., et al. 2005, A&A, 444, 365
Willis, J. P., Pacaud, F., Valtchanov, I., et al. 2005, MNRAS, 363, 675
Wilman, D. J., Oemler, A., Mulchaey, J. S., et al. 2009, ApJ, 692, 298
Wolf, C., Gray, M. E., Aragón-Salamanca, A., Lane, K. P., & Meisenheimer, K. 2007, MNRAS, 376, L1
Zabludoff, A. I., & Mulchaey, J. S. 1998, ApJ, 496, 39

[1] National Research Council of Canada, Herzberg Institute of Astrophysics, 5071 West Saanich Road, Victoria, British Columbia, Canada
[2] Ohio University, Department of Physics and Astronomy, Clippinger Lab 251B, Athens, OH 45701, USA
[3] California Institute of Technology, MS 320-47, Pasadena, CA 91125, USA
[4] University of Washington, Department of Astronomy, Box 351580, Seattle, WA 98195-1580, USA
[5] Kavli Institute for Particle Astrophysics and Cosmology, PO Box 20450, MS 29, Stanford, CA 94309, USA
[6] Max-Planck-Institut für Astrophysik, Karl-Schwarschild-Str. 1, Postfach 1317, 85741 Garching, Germany
[7] INAF – Astronomical Observatory of Padova, Italy
[8] School of Physics and Astronomy, University of Nottingham, Nottingham, NG7 2RD, UK
[9] INAF – Astronomical Observatory of Trieste, via Tiepolo 11, 34143 Trieste, Italy
[10] INAF – Osservatorio Astronomico di Arcetri, Largo Enrico Fermi 5, 50125 Firenze, Italy
[11] Observatoire de l'Université de Genève, Laboratoire d'Astrophysique de l'École Polytechnique Fédérale de Lausanne (EPFL), 1290 Sauverny, Switzerland
[12] Dark Cosmology Centre, Niels Bohr Institute, University of Copenhagen, Juliane Maries Vej 30, 2100 Copenhagen, Denmark
[13] The Royal Library/Copenhagen University Library, Research Department, Box 2149, 1016 Copenhagen K, Denmark
[14] Max-Planck Institut für extraterrestrische Physik, Giessenbachstrasse 85748 Garching, Germany
[15] Laboratoire d'Astrophysique de Toulouse-Tarbes, CNRS, Université de Toulouse, 14 avenue Édouard Belin, 31400 Toulouse, France
[16] The University of Kansas, Department of Physics and Astronomy, Malott room 1082, 1251 Wescoe Hall Drive, Lawrence, KS, 66045, USA
[17] NOAO, 950 North Cherry Avenue, Tucson, AZ 85719, USA
[18] Steward Observatory, University of Arizona, 933 North Cherry Avenue, Tucson, AZ, 85721, USA

**Table 4.** Velocity-dispersion-matched sample of 158 SDSS clusters in order of decreasing velocity dispersion.

| SDSS C4[3] ID | $z$ | $N$[4] | $\sigma_v$ (km s$^{-1}$) | $R_{200}$ (Mpc) | $M_{\rm cl}$ ($10^{15} M_\odot$) | $R \leq 0.6R_{200}$ | | | |
|---|---|---|---|---|---|---|---|---|---|
| | | | | | | $f_{\rm et,raw}$ | $f_{\rm et,corr}$ | $f_{\rm [OII],raw}$ | $f_{\rm [OII],corr}$ |
| (1) | (2) | (3) | (4) | (5) | (6) | (7) | (8) | (9) | (10) |
| 3004 | 0.0801 | 199 | 1156 ± 61 | 2.75 | 2.550 | 0.69 ± 0.04 | 0.69 ± 0.04 | 0.27 ± 0.04 | 0.30 ± 0.04 |
| 2035 | 0.0652 | 77 | 1084 ± 114 | 2.60 | 2.117 | 0.38 ± 0.11 | 0.41 ± 0.12 | 0.67 ± 0.11 | 0.69 ± 0.11 |
| 1004 | 0.0774 | 127 | 966 ± 59 | 2.30 | 1.491 | 0.77 ± 0.04 | 0.73 ± 0.05 | 0.14 ± 0.04 | 0.15 ± 0.04 |
| 2026 | 0.0444 | 147 | 933 ± 71 | 2.26 | 1.364 | 0.56 ± 0.10 | 0.54 ± 0.10 | 0.18 ± 0.07 | 0.18 ± 0.07 |
| 2159 | 0.0563 | 44 | 915 ± 69 | 2.20 | 1.281 | 0.28 ± 0.12 | 0.21 ± 0.12 | 0.65 ± 0.13 | 0.67 ± 0.13 |
| 2013 | 0.0556 | 160 | 903 ± 56 | 2.18 | 1.231 | 0.70 ± 0.06 | 0.70 ± 0.06 | 0.08 ± 0.03 | 0.09 ± 0.04 |
| 3347 | 0.0759 | 30 | 902 ± 102 | 2.15 | 1.216 | 0.50 ± 0.12 | 0.46 ± 0.12 | 0.50 ± 0.12 | 0.53 ± 0.12 |
| 3500 | 0.0783 | 18 | 892 ± 113 | 2.13 | 1.174 | 0.50 ± 0.14 | 0.41 ± 0.14 | 0.59 ± 0.14 | 0.66 ± 0.14 |
| 1126 | 0.0843 | 57 | 878 ± 77 | 2.08 | 1.113 | 0.62 ± 0.08 | 0.67 ± 0.08 | 0.17 ± 0.06 | 0.18 ± 0.07 |
| 3028 | 0.0704 | 121 | 872 ± 54 | 2.09 | 1.101 | 0.69 ± 0.08 | 0.71 ± 0.08 | 0.21 ± 0.07 | 0.22 ± 0.08 |
| 1389 | 0.0801 | 16 | 853 ± 134 | 2.03 | 1.024 | 0.71 ± 0.26 | 1.00 ± 0.26 | 0.29 ± 0.26 | 0.00 ± 0.26 |
| 1048 | 0.0774 | 75 | 828 ± 78 | 1.97 | 0.937 | 0.60 ± 0.07 | 0.59 ± 0.07 | 0.22 ± 0.06 | 0.20 ± 0.06 |
| 3016 | 0.0497 | 101 | 822 ± 54 | 1.98 | 0.929 | 0.60 ± 0.08 | 0.60 ± 0.08 | 0.47 ± 0.08 | 0.50 ± 0.08 |
| 2002 | 0.0762 | 102 | 812 ± 49 | 1.94 | 0.885 | 0.63 ± 0.06 | 0.58 ± 0.06 | 0.28 ± 0.05 | 0.30 ± 0.06 |
| 1002 | 0.0690 | 90 | 800 ± 56 | 1.92 | 0.851 | 0.57 ± 0.07 | 0.55 ± 0.07 | 0.28 ± 0.06 | 0.30 ± 0.06 |
| 1025 | 0.0451 | 66 | 790 ± 54 | 1.91 | 0.827 | 0.68 ± 0.09 | 0.67 ± 0.10 | 0.15 ± 0.07 | 0.16 ± 0.08 |
| 3084 | 0.0607 | 65 | 781 ± 70 | 1.88 | 0.795 | 0.52 ± 0.10 | 0.51 ± 0.10 | 0.37 ± 0.09 | 0.36 ± 0.09 |
| 1044 | 0.0837 | 60 | 771 ± 79 | 1.83 | 0.755 | 0.72 ± 0.07 | 0.73 ± 0.07 | 0.12 ± 0.05 | 0.11 ± 0.05 |
| 2074 | 0.0787 | 21 | 765 ± 99 | 1.82 | 0.740 | 0.24 ± 0.11 | 0.29 ± 0.11 | 0.63 ± 0.12 | 0.63 ± 0.12 |
| 2050 | 0.0588 | 62 | 759 ± 59 | 1.83 | 0.730 | 0.42 ± 0.19 | 0.41 ± 0.36 | 0.58 ± 0.19 | 0.62 ± 0.33 |
| 1058 | 0.0831 | 68 | 749 ± 63 | 1.78 | 0.692 | 0.58 ± 0.07 | 0.55 ± 0.07 | 0.19 ± 0.05 | 0.21 ± 0.06 |
| 1401 | 0.0643 | 28 | 748 ± 97 | 1.79 | 0.696 | 0.40 ± 0.13 | 0.34 ± 0.12 | 0.47 ± 0.13 | 0.46 ± 0.13 |
| 1001 | 0.0794 | 82 | 746 ± 58 | 1.78 | 0.687 | 0.74 ± 0.06 | 0.74 ± 0.06 | 0.15 ± 0.05 | 0.15 ± 0.05 |
| 2015 | 0.0797 | 59 | 742 ± 77 | 1.77 | 0.675 | 0.61 ± 0.08 | 0.59 ± 0.08 | 0.29 ± 0.07 | 0.29 ± 0.07 |
| 1276 | 0.0810 | 17 | 729 ± 79 | 1.73 | 0.639 | 0.43 ± 0.13 | 0.40 ± 0.13 | 0.72 ± 0.12 | 0.76 ± 0.12 |
| 3065 | 0.0649 | 83 | 724 ± 54 | 1.74 | 0.631 | 0.66 ± 0.08 | 0.67 ± 0.08 | 0.23 ± 0.07 | 0.21 ± 0.07 |
| 1069 | 0.0764 | 59 | 721 ± 69 | 1.72 | 0.621 | 0.53 ± 0.09 | 0.54 ± 0.09 | 0.26 ± 0.08 | 0.24 ± 0.08 |
| 2069 | 0.0746 | 22 | 720 ± 119 | 1.72 | 0.619 | 0.50 ± 0.34 | 0.00 ± 0.34 | 0.50 ± 0.34 | 1.00 ± 0.34 |
| 2001 | 0.0417 | 125 | 695 ± 52 | 1.68 | 0.564 | 0.68 ± 0.09 | 0.70 ± 0.09 | 0.24 ± 0.08 | 0.24 ± 0.08 |
| 3630 | 0.0682 | 18 | 693 ± 78 | 1.66 | 0.553 | 0.44 ± 0.16 | 0.41 ± 0.17 | 0.68 ± 0.15 | 0.73 ± 0.16 |
| 1291 | 0.0557 | 25 | 685 ± 84 | 1.65 | 0.537 | 0.50 ± 0.34 | 0.71 ± 0.34 | 0.50 ± 0.34 | 0.00 ± 0.34 |
| 3018 | 0.0517 | 85 | 684 ± 52 | 1.65 | 0.535 | 0.36 ± 0.08 | 0.38 ± 0.09 | 0.27 ± 0.08 | 0.27 ± 0.08 |
| 3404 | 0.0750 | 19 | 683 ± 101 | 1.63 | 0.527 | 0.78 ± 0.11 | 0.81 ± 0.12 | 0.30 ± 0.13 | 0.29 ± 0.13 |
| 1041 | 0.0758 | 62 | 678 ± 68 | 1.62 | 0.516 | 0.70 ± 0.08 | 0.70 ± 0.08 | 0.19 ± 0.06 | 0.18 ± 0.07 |
| 1372 | 0.0804 | 34 | 677 ± 51 | 1.61 | 0.513 | 0.74 ± 0.11 | 0.78 ± 0.11 | 0.26 ± 0.11 | 0.23 ± 0.11 |
| 3055 | 0.0581 | 29 | 675 ± 82 | 1.62 | 0.513 | 0.64 ± 0.10 | 0.63 ± 0.10 | 0.36 ± 0.10 | 0.39 ± 0.10 |
| 3027 | 0.0737 | 38 | 670 ± 74 | 1.60 | 0.498 | 0.76 ± 0.09 | 0.78 ± 0.09 | 0.11 ± 0.06 | 0.09 ± 0.07 |
| 1172 | 0.0793 | 23 | 670 ± 130 | 1.60 | 0.497 | 0.41 ± 0.14 | 0.33 ± 0.14 | 0.32 ± 0.13 | 0.29 ± 0.14 |
| 3531 | 0.0635 | 17 | 660 ± 115 | 1.58 | 0.479 | 0.69 ± 0.19 | 0.80 ± 0.19 | 0.13 ± 0.14 | 0.00 ± 0.14 |
| 3140 | 0.0449 | 42 | 637 ± 84 | 1.54 | 0.435 | 0.44 ± 0.16 | 0.41 ± 0.17 | 0.56 ± 0.16 | 0.55 ± 0.17 |
| 3050 | 0.0734 | 46 | 635 ± 67 | 1.52 | 0.424 | 0.71 ± 0.10 | 0.72 ± 0.10 | 0.34 ± 0.11 | 0.32 ± 0.11 |
| 1170 | 0.0846 | 23 | 633 ± 83 | 1.50 | 0.418 | 0.81 ± 0.09 | 0.85 ± 0.09 | 0.24 ± 0.10 | 0.19 ± 0.09 |
| 1011 | 0.0847 | 36 | 631 ± 73 | 1.50 | 0.415 | 0.56 ± 0.12 | 0.58 ± 0.12 | 0.33 ± 0.11 | 0.29 ± 0.11 |
| 3123 | 0.0583 | 12 | 629 ± 146 | 1.51 | 0.416 | 0.36 ± 0.17 | 0.32 ± 0.17 | 0.50 ± 0.18 | 0.54 ± 0.18 |
| 2004 | 0.0579 | 93 | 627 ± 42 | 1.51 | 0.411 | 0.70 ± 0.08 | 0.71 ± 0.08 | 0.36 ± 0.08 | 0.36 ± 0.08 |
| 3043 | 0.0698 | 54 | 621 ± 62 | 1.49 | 0.398 | 0.60 ± 0.08 | 0.60 ± 0.08 | 0.29 ± 0.07 | 0.29 ± 0.08 |
| 3478 | 0.0741 | 14 | 617 ± 75 | 1.47 | 0.388 | 0.45 ± 0.15 | 0.45 ± 0.15 | 0.55 ± 0.15 | 0.56 ± 0.15 |
| 1275 | 0.0721 | 18 | 617 ± 132 | 1.48 | 0.390 | 0.41 ± 0.14 | 0.37 ± 0.14 | 0.76 ± 0.12 | 0.83 ± 0.12 |
| 3020 | 0.0629 | 30 | 613 ± 79 | 1.47 | 0.383 | 0.43 ± 0.10 | 0.43 ± 0.10 | 0.39 ± 0.10 | 0.40 ± 0.10 |
| 3319 | 0.0639 | 21 | 601 ± 40 | 1.44 | 0.361 | 0.35 ± 0.13 | 0.32 ± 0.13 | 0.57 ± 0.13 | 0.59 ± 0.13 |
| 3529 | 0.0410 | 19 | 596 ± 141 | 1.45 | 0.357 | 0.58 ± 0.19 | 0.55 ± 0.19 | 0.42 ± 0.19 | 0.45 ± 0.19 |
| 2018 | 0.0550 | 65 | 596 ± 54 | 1.44 | 0.353 | 0.69 ± 0.10 | 0.68 ± 0.10 | 0.13 ± 0.07 | 0.12 ± 0.07 |
| 1017 | 0.0769 | 41 | 596 ± 56 | 1.42 | 0.350 | 0.83 ± 0.07 | 0.85 ± 0.07 | 0.06 ± 0.05 | 0.04 ± 0.05 |
| 1088 | 0.0735 | 32 | 591 ± 74 | 1.41 | 0.343 | 0.65 ± 0.11 | 0.71 ± 0.11 | 0.16 ± 0.09 | 0.13 ± 0.09 |
| 1026 | 0.0720 | 26 | 580 ± 74 | 1.39 | 0.323 | 0.41 ± 0.14 | 0.42 ± 0.14 | 0.59 ± 0.14 | 0.61 ± 0.14 |
| 1024 | 0.0826 | 37 | 579 ± 89 | 1.38 | 0.320 | 0.50 ± 0.34 | 0.48 ± 0.34 | 0.50 ± 0.34 | 0.45 ± 0.34 |
| 3064 | 0.0610 | 42 | 577 ± 68 | 1.39 | 0.320 | 0.34 ± 0.10 | 0.33 ± 0.10 | 0.70 ± 0.09 | 0.72 ± 0.10 |
| 2009 | 0.0530 | 42 | 573 ± 54 | 1.38 | 0.315 | 0.59 ± 0.10 | 0.61 ± 0.11 | 0.36 ± 0.10 | 0.32 ± 0.10 |
| 3275 | 0.0699 | 12 | 570 ± 133 | 1.36 | 0.307 | 0.32 ± 0.15 | 0.24 ± 0.16 | 0.80 ± 0.13 | 0.90 ± 0.13 |
| 3088 | 0.0463 | 61 | 556 ± 61 | 1.34 | 0.288 | 0.63 ± 0.12 | 0.63 ± 0.12 | 0.17 ± 0.09 | 0.14 ± 0.09 |

**Table 4.** continued.

| SDSS C4[5] ID | $z$ | $N$[6] | $\sigma_v$ | $R_{200}$ | $M_{\rm cl}$ | $R \leq 0.6R_{200}$ | | | |
|---|---|---|---|---|---|---|---|---|---|
| | | | (km s$^{-1}$) | (Mpc) | ($10^{15} M_\odot$) | $f_{\rm et,raw}$ | $f_{\rm et,corr}$ | $f_{\rm [OII],raw}$ | $f_{\rm [OII],corr}$ |
| (1) | (2) | (3) | (4) | (5) | (6) | (7) | (8) | (9) | (10) |
| 3023 | 0.0719 | 47 | 556 ± 51 | 1.33 | 0.285 | 0.62 ± 0.09 | 0.62 ± 0.10 | 0.18 ± 0.08 | 0.20 ± 0.08 |
| 3041 | 0.0776 | 15 | 555 ± 72 | 1.32 | 0.283 | 0.45 ± 0.15 | 0.46 ± 0.15 | 0.45 ± 0.15 | 0.45 ± 0.15 |
| 2016 | 0.0449 | 135 | 552 ± 34 | 1.34 | 0.283 | 0.42 ± 0.09 | 0.41 ± 0.09 | 0.33 ± 0.08 | 0.31 ± 0.08 |
| 3474 | 0.0519 | 19 | 547 ± 93 | 1.32 | 0.275 | 0.32 ± 0.15 | 0.27 ± 0.16 | 0.44 ± 0.16 | 0.48 ± 0.17 |
| 3505 | 0.0711 | 18 | 543 ± 96 | 1.30 | 0.266 | 0.55 ± 0.15 | 0.55 ± 0.15 | 0.45 ± 0.15 | 0.50 ± 0.15 |
| 3237 | 0.0456 | 30 | 542 ± 66 | 1.31 | 0.267 | 0.85 ± 0.10 | 0.90 ± 0.10 | 0.32 ± 0.13 | 0.30 ± 0.14 |
| 3249 | 0.0740 | 19 | 541 ± 98 | 1.29 | 0.263 | 0.60 ± 0.13 | 0.63 ± 0.13 | 0.47 ± 0.13 | 0.45 ± 0.13 |
| 3117 | 0.0623 | 49 | 536 ± 52 | 1.29 | 0.257 | 0.72 ± 0.10 | 0.75 ± 0.10 | 0.13 ± 0.07 | 0.08 ± 0.07 |
| 3003 | 0.0597 | 59 | 535 ± 56 | 1.29 | 0.255 | 0.61 ± 0.09 | 0.62 ± 0.09 | 0.35 ± 0.09 | 0.35 ± 0.09 |
| 3121 | 0.0627 | 29 | 529 ± 71 | 1.27 | 0.247 | 0.63 ± 0.12 | 0.62 ± 0.12 | 0.30 ± 0.11 | 0.31 ± 0.12 |
| 3167 | 0.0732 | 19 | 526 ± 82 | 1.26 | 0.240 | 0.70 ± 0.13 | 0.71 ± 0.13 | 0.38 ± 0.13 | 0.37 ± 0.13 |
| 2058 | 0.0734 | 21 | 526 ± 99 | 1.26 | 0.241 | 0.54 ± 0.14 | 0.52 ± 0.14 | 0.38 ± 0.13 | 0.39 ± 0.14 |
| 3011 | 0.0820 | 26 | 524 ± 81 | 1.25 | 0.237 | 0.66 ± 0.11 | 0.66 ± 0.11 | 0.24 ± 0.10 | 0.23 ± 0.10 |
| 3015 | 0.0689 | 34 | 523 ± 67 | 1.25 | 0.238 | 0.59 ± 0.10 | 0.59 ± 0.10 | 0.36 ± 0.10 | 0.35 ± 0.10 |
| 2178 | 0.0526 | 14 | 522 ± 84 | 1.26 | 0.238 | 0.26 ± 0.17 | 0.21 ± 0.17 | 0.58 ± 0.19 | 0.60 ± 0.19 |
| 1047 | 0.0829 | 22 | 521 ± 87 | 1.24 | 0.233 | 0.92 ± 0.09 | 1.00 ± 0.09 | 0.08 ± 0.09 | 0.00 ± 0.09 |
| 1120 | 0.0756 | 13 | 516 ± 109 | 1.23 | 0.227 | 0.44 ± 0.16 | 0.41 ± 0.17 | 0.44 ± 0.16 | 0.44 ± 0.17 |
| 1050 | 0.0717 | 14 | 514 ± 88 | 1.23 | 0.225 | 0.68 ± 0.13 | 0.65 ± 0.14 | 0.41 ± 0.14 | 0.44 ± 0.14 |
| 3583 | 0.0673 | 29 | 512 ± 80 | 1.23 | 0.223 | 0.64 ± 0.10 | 0.63 ± 0.10 | 0.31 ± 0.10 | 0.31 ± 0.10 |
| 3196 | 0.0603 | 17 | 512 ± 92 | 1.23 | 0.224 | 0.29 ± 0.14 | 0.26 ± 0.14 | 0.50 ± 0.16 | 0.51 ± 0.16 |
| 2005 | 0.0433 | 48 | 506 ± 47 | 1.23 | 0.218 | 0.84 ± 0.11 | 0.91 ± 0.11 | 0.16 ± 0.11 | 0.11 ± 0.11 |
| 1223 | 0.0600 | 18 | 506 ± 50 | 1.22 | 0.216 | 0.50 ± 0.34 | 0.74 ± 0.34 | 0.50 ± 0.34 | 0.41 ± 0.34 |
| 2020 | 0.0740 | 32 | 505 ± 83 | 1.21 | 0.213 | 0.68 ± 0.15 | 0.71 ± 0.15 | 0.08 ± 0.09 | 0.00 ± 0.09 |
| 1179 | 0.0775 | 16 | 505 ± 94 | 1.20 | 0.212 | 0.50 ± 0.14 | 0.45 ± 0.14 | 0.50 ± 0.14 | 0.56 ± 0.14 |
| 3539 | 0.0542 | 12 | 502 ± 122 | 1.21 | 0.212 | 0.21 ± 0.20 | 0.00 ± 0.20 | 0.50 ± 0.25 | 0.56 ± 0.25 |
| 3080 | 0.0616 | 17 | 501 ± 110 | 1.20 | 0.209 | 0.68 ± 0.15 | 0.74 ± 0.16 | 0.32 ± 0.15 | 0.25 ± 0.16 |
| 2111 | 0.0778 | 8 | 500 ± 172 | 1.19 | 0.207 | 0.50 ± 0.34 | 0.77 ± 0.34 | 0.50 ± 0.34 | 0.00 ± 0.34 |
| 1149 | 0.0523 | 33 | 500 ± 62 | 1.21 | 0.209 | 0.45 ± 0.15 | 0.46 ± 0.15 | 0.55 ± 0.15 | 0.53 ± 0.15 |
| 1404 | 0.0789 | 14 | 498 ± 155 | 1.19 | 0.204 | 0.44 ± 0.16 | 0.35 ± 0.16 | 0.56 ± 0.16 | 0.66 ± 0.16 |
| 1144 | 0.0751 | 20 | 497 ± 71 | 1.19 | 0.203 | 0.71 ± 0.14 | 0.71 ± 0.14 | 0.29 ± 0.14 | 0.29 ± 0.14 |
| 1147 | 0.0809 | 17 | 493 ± 95 | 1.17 | 0.197 | 0.68 ± 0.13 | 0.69 ± 0.13 | 0.15 ± 0.10 | 0.14 ± 0.10 |
| 3019 | 0.0682 | 32 | 492 ± 67 | 1.18 | 0.198 | 0.74 ± 0.11 | 0.78 ± 0.11 | 0.53 ± 0.13 | 0.54 ± 0.13 |
| 1178 | 0.0543 | 32 | 490 ± 41 | 1.18 | 0.197 | 0.54 ± 0.14 | 0.51 ± 0.14 | 0.54 ± 0.14 | 0.60 ± 0.13 |
| 3066 | 0.0767 | 30 | 482 ± 49 | 1.15 | 0.185 | 0.61 ± 0.10 | 0.62 ± 0.10 | 0.30 ± 0.09 | 0.24 ± 0.09 |
| 2027 | 0.0790 | 34 | 481 ± 62 | 1.14 | 0.184 | 0.50 ± 0.34 | 0.54 ± 0.34 | 0.50 ± 0.34 | 0.18 ± 0.34 |
| 3344 | 0.0738 | 8 | 479 ± 63 | 1.14 | 0.182 | 0.80 ± 0.13 | 0.78 ± 0.16 | 0.32 ± 0.15 | 0.35 ± 0.16 |
| 3083 | 0.0760 | 19 | 470 ± 64 | 1.12 | 0.172 | 0.50 ± 0.13 | 0.53 ± 0.13 | 0.50 ± 0.13 | 0.48 ± 0.13 |
| 1087 | 0.0782 | 15 | 465 ± 180 | 1.11 | 0.166 | 0.37 ± 0.12 | 0.37 ± 0.12 | 0.63 ± 0.12 | 0.60 ± 0.12 |
| 1005 | 0.0809 | 21 | 458 ± 50 | 1.09 | 0.159 | 0.50 ± 0.20 | 0.50 ± 0.20 | 0.31 ± 0.19 | 0.25 ± 0.19 |
| 1360 | 0.0746 | 8 | 448 ± 103 | 1.07 | 0.149 | 0.23 ± 0.15 | 0.18 ± 0.15 | 0.77 ± 0.15 | 0.84 ± 0.15 |
| 3120 | 0.0731 | 19 | 445 ± 80 | 1.06 | 0.146 | 0.70 ± 0.13 | 0.70 ± 0.13 | 0.38 ± 0.13 | 0.38 ± 0.13 |
| 3248 | 0.0446 | 20 | 442 ± 90 | 1.07 | 0.145 | 0.26 ± 0.17 | 0.27 ± 0.17 | 0.58 ± 0.19 | 0.56 ± 0.19 |
| 3069 | 0.0555 | 20 | 441 ± 47 | 1.06 | 0.144 | 0.76 ± 0.12 | 0.82 ± 0.12 | 0.41 ± 0.14 | 0.39 ± 0.14 |
| 2121 | 0.0817 | 13 | 441 ± 86 | 1.05 | 0.141 | 0.42 ± 0.19 | 0.37 ± 0.19 | 0.58 ± 0.19 | 0.63 ± 0.19 |
| 2141 | 0.0779 | 16 | 422 ± 89 | 1.00 | 0.124 | 0.80 ± 0.13 | 0.87 ± 0.13 | 0.20 ± 0.13 | 0.11 ± 0.13 |
| 3506 | 0.0635 | 11 | 421 ± 87 | 1.01 | 0.124 | 0.26 ± 0.17 | 0.22 ± 0.17 | 0.74 ± 0.17 | 0.79 ± 0.17 |
| 1368 | 0.0520 | 10 | 417 ± 91 | 1.01 | 0.121 | 0.61 ± 0.22 | 0.72 ± 0.22 | 0.39 ± 0.22 | 0.28 ± 0.22 |
| 2052 | 0.0772 | 12 | 415 ± 72 | 0.99 | 0.118 | 0.50 ± 0.14 | 0.49 ± 0.14 | 0.15 ± 0.10 | 0.10 ± 0.10 |
| 2000 | 0.0699 | 29 | 411 ± 53 | 0.98 | 0.115 | 0.48 ± 0.10 | 0.48 ± 0.10 | 0.43 ± 0.10 | 0.43 ± 0.10 |
| 1009 | 0.0746 | 27 | 404 ± 41 | 0.97 | 0.110 | 0.53 ± 0.11 | 0.52 ± 0.11 | 0.31 ± 0.11 | 0.33 ± 0.11 |
| 3146 | 0.0459 | 24 | 403 ± 45 | 0.97 | 0.110 | 0.55 ± 0.15 | 0.53 ± 0.15 | 0.07 ± 0.08 | 0.00 ± 0.08 |
| 1043 | 0.0743 | 30 | 403 ± 60 | 0.96 | 0.109 | 0.74 ± 0.11 | 0.79 ± 0.11 | 0.26 ± 0.11 | 0.22 ± 0.11 |
| 1106 | 0.0402 | 18 | 402 ± 112 | 0.98 | 0.109 | 0.39 ± 0.15 | 0.34 ± 0.15 | 0.50 ± 0.16 | 0.44 ± 0.16 |
| 3572 | 0.0587 | 11 | 393 ± 183 | 0.95 | 0.102 | 0.79 ± 0.20 | 1.00 ± 0.20 | 0.21 ± 0.20 | 0.00 ± 0.20 |
| 3144 | 0.0805 | 16 | 386 ± 57 | 0.92 | 0.095 | 0.94 ± 0.06 | 1.00 ± 0.06 | 0.14 ± 0.09 | 0.08 ± 0.10 |
| 2010 | 0.0645 | 18 | 384 ± 55 | 0.92 | 0.095 | 0.50 ± 0.18 | 0.46 ± 0.18 | 0.36 ± 0.17 | 0.36 ± 0.17 |
| 2211 | 0.0422 | 22 | 372 ± 38 | 0.90 | 0.087 | 0.68 ± 0.15 | 0.74 ± 0.16 | 0.32 ± 0.15 | 0.31 ± 0.16 |
| 1341 | 0.0700 | 10 | 370 ± 59 | 0.88 | 0.084 | 0.58 ± 0.19 | 0.56 ± 0.19 | 0.26 ± 0.17 | 0.21 ± 0.17 |
| 3388 | 0.0722 | 12 | 357 ± 109 | 0.85 | 0.075 | 0.61 ± 0.22 | 0.66 ± 0.22 | 0.61 ± 0.22 | 0.63 ± 0.22 |
| 3007 | 0.0685 | 32 | 356 ± 50 | 0.85 | 0.075 | 0.73 ± 0.09 | 0.74 ± 0.09 | 0.17 ± 0.08 | 0.13 ± 0.08 |
| 2140 | 0.0810 | 5 | 355 ± 216 | 0.84 | 0.074 | 0.13 ± 0.14 | 0.00 ± 0.14 | 0.87 ± 0.14 | 1.00 ± 0.14 |

**Table 4.** continued.

| SDSS C4[7] ID | $z$ | $N$[8] | $\sigma_v$ | $R_{200}$ | $M_{\rm cl}$ | $R \leq 0.6R_{200}$ | | | |
|---|---|---|---|---|---|---|---|---|---|
| | | | (km s$^{-1}$) | (Mpc) | ($10^{15} M_\odot$) | $f_{\rm et,raw}$ | $f_{\rm et,corr}$ | $f_{\rm [OII],raw}$ | $f_{\rm [OII],corr}$ |
| (1) | (2) | (3) | (4) | (5) | (6) | (7) | (8) | (9) | (10) |
| 3182 | 0.0614 | 18 | 352 ± 84 | 0.85 | 0.073 | 0.44 ± 0.16 | 0.42 ± 0.17 | 0.20 ± 0.13 | 0.16 ± 0.13 |
| 1006 | 0.0477 | 24 | 340 ± 54 | 0.82 | 0.066 | 0.77 ± 0.15 | 0.85 ± 0.15 | 0.23 ± 0.15 | 0.15 ± 0.15 |
| 2120 | 0.0518 | 12 | 338 ± 101 | 0.82 | 0.065 | 0.58 ± 0.19 | 0.58 ± 0.19 | 0.42 ± 0.19 | 0.41 ± 0.19 |
| 3341 | 0.0723 | 14 | 331 ± 97 | 0.79 | 0.060 | 0.56 ± 0.16 | 0.55 ± 0.17 | 0.32 ± 0.15 | 0.30 ± 0.16 |
| 3272 | 0.0692 | 9 | 329 ± 54 | 0.79 | 0.059 | 0.69 ± 0.19 | 0.72 ± 0.19 | 0.50 ± 0.20 | 0.55 ± 0.20 |
| 2156 | 0.0668 | 17 | 328 ± 50 | 0.79 | 0.059 | 0.82 ± 0.12 | 0.89 ± 0.12 | 0.18 ± 0.12 | 0.11 ± 0.12 |
| 1015 | 0.0792 | 10 | 327 ± 66 | 0.78 | 0.058 | 0.79 ± 0.20 | 1.00 ± 0.20 | 0.50 ± 0.25 | 0.57 ± 0.25 |
| 2122 | 0.0826 | 7 | 315 ± 61 | 0.75 | 0.052 | 0.42 ± 0.19 | 0.31 ± 0.19 | 0.42 ± 0.19 | 0.31 ± 0.19 |
| 3340 | 0.0611 | 8 | 314 ± 60 | 0.75 | 0.051 | 0.79 ± 0.20 | 1.00 ± 0.20 | 0.21 ± 0.20 | 0.00 ± 0.20 |
| 3247 | 0.0571 | 14 | 307 ± 97 | 0.74 | 0.048 | 0.29 ± 0.26 | 0.00 ± 0.26 | 0.71 ± 0.26 | 1.00 ± 0.26 |
| 3061 | 0.0480 | 21 | 300 ± 37 | 0.72 | 0.045 | 0.58 ± 0.19 | 0.58 ± 0.19 | 0.42 ± 0.19 | 0.37 ± 0.19 |
| 1040 | 0.0539 | 16 | 299 ± 38 | 0.72 | 0.045 | 0.39 ± 0.22 | 0.40 ± 0.22 | 0.39 ± 0.22 | 0.36 ± 0.22 |
| 3267 | 0.0710 | 5 | 298 ± 147 | 0.71 | 0.044 | 0.31 ± 0.19 | 0.20 ± 0.19 | 0.50 ± 0.20 | 0.50 ± 0.20 |
| 3328 | 0.0412 | 12 | 297 ± 40 | 0.72 | 0.044 | 0.50 ± 0.25 | 0.54 ± 0.25 | 0.50 ± 0.25 | 0.43 ± 0.25 |
| 2070 | 0.0775 | 12 | 295 ± 52 | 0.70 | 0.043 | 0.56 ± 0.16 | 0.57 ± 0.17 | 0.44 ± 0.16 | 0.42 ± 0.17 |
| 3169 | 0.0756 | 7 | 291 ± 146 | 0.70 | 0.041 | 0.32 ± 0.15 | 0.30 ± 0.16 | 0.80 ± 0.13 | 0.91 ± 0.13 |
| 3262 | 0.0452 | 32 | 282 ± 48 | 0.68 | 0.038 | 0.61 ± 0.22 | 0.67 ± 0.22 | 0.61 ± 0.22 | 0.74 ± 0.22 |
| 1297 | 0.0451 | 10 | 271 ± 85 | 0.66 | 0.033 | 0.39 ± 0.22 | 0.27 ± 0.22 | 0.39 ± 0.22 | 0.33 ± 0.22 |
| 3147 | 0.0534 | 11 | 265 ± 80 | 0.64 | 0.031 | 0.69 ± 0.19 | 0.82 ± 0.19 | 0.13 ± 0.14 | 0.00 ± 0.14 |
| 1128 | 0.0619 | 12 | 257 ± 64 | 0.62 | 0.028 | 0.64 ± 0.17 | 0.66 ± 0.17 | 0.36 ± 0.17 | 0.35 ± 0.17 |
| 3062 | 0.0615 | 12 | 256 ± 44 | 0.62 | 0.028 | 0.56 ± 0.16 | 0.55 ± 0.17 | 0.44 ± 0.16 | 0.45 ± 0.17 |
| 3318 | 0.0419 | 7 | 252 ± 56 | 0.61 | 0.027 | 0.50 ± 0.20 | 0.48 ± 0.21 | 0.50 ± 0.20 | 0.51 ± 0.20 |
| 1171 | 0.0556 | 15 | 242 ± 48 | 0.58 | 0.024 | 0.61 ± 0.22 | 0.67 ± 0.22 | 0.39 ± 0.22 | 0.33 ± 0.22 |
| 1384 | 0.0541 | 7 | 240 ± 55 | 0.58 | 0.023 | 0.71 ± 0.26 | 1.00 ± 0.26 | 0.29 ± 0.26 | 0.00 ± 0.26 |
| 3581 | 0.0591 | 5 | 236 ± 57 | 0.57 | 0.022 | 0.50 ± 0.25 | 0.38 ± 0.25 | 0.79 ± 0.20 | 1.00 ± 0.20 |
| 3407 | 0.0652 | 4 | 233 ± 107 | 0.56 | 0.021 | 0.29 ± 0.26 | 0.00 ± 0.26 | 0.29 ± 0.26 | 0.00 ± 0.26 |
| 2150 | 0.0415 | 9 | 221 ± 66 | 0.53 | 0.018 | 0.50 ± 0.34 | 0.13 ± 0.34 | 0.50 ± 0.34 | 0.71 ± 0.34 |
| 2112 | 0.0510 | 12 | 212 ± 59 | 0.51 | 0.016 | 0.71 ± 0.26 | 1.00 ± 0.26 | 0.29 ± 0.26 | 0.00 ± 0.26 |
| 3553 | 0.0434 | 10 | 208 ± 53 | 0.50 | 0.015 | 0.61 ± 0.22 | 0.67 ± 0.22 | 0.61 ± 0.22 | 0.63 ± 0.22 |
| 3195 | 0.0599 | 11 | 206 ± 31 | 0.50 | 0.015 | 0.69 ± 0.19 | 0.72 ± 0.19 | 0.50 ± 0.20 | 0.60 ± 0.21 |
| 3052 | 0.0746 | 7 | 202 ± 77 | 0.48 | 0.014 | 0.50 ± 0.20 | 0.47 ± 0.20 | 0.31 ± 0.19 | 0.27 ± 0.19 |
| 1344 | 0.0747 | 7 | 202 ± 47 | 0.48 | 0.014 | 0.77 ± 0.15 | 0.84 ± 0.15 | 0.50 ± 0.18 | 0.56 ± 0.18 |
| 3428 | 0.0730 | 5 | 193 ± 41 | 0.46 | 0.012 | 0.39 ± 0.22 | 0.34 ± 0.22 | 0.61 ± 0.22 | 0.65 ± 0.22 |
| 3345 | 0.0516 | 4 | 142 ± 57 | 0.34 | 0.005 | 0.71 ± 0.26 | 1.00 ± 0.26 | 0.29 ± 0.26 | 0.00 ± 0.26 |
| 3265 | 0.0597 | 4 | 142 ± 11 | 0.34 | 0.005 | 0.50 ± 0.25 | 0.43 ± 0.25 | 0.50 ± 0.25 | 0.43 ± 0.25 |
| 3355 | 0.0677 | 4 | 125 ± 61 | 0.30 | 0.003 | 0.84 ± 0.16 | 1.00 ± 0.16 | 0.16 ± 0.16 | 0.00 ± 0.16 |
| 3244 | 0.0600 | 4 | 120 ± 20 | 0.29 | 0.003 | 0.71 ± 0.26 | 1.00 ± 0.26 | 0.71 ± 0.26 | 1.00 ± 0.26 |

[3] From von der Linden (2007); [4] number of spectroscopically-confirmed cluster members from von der Linden (2007).